

Isospin magnetic texture and intervalley exchange interaction in rhombohedral tetralayer graphene

Received: 5 October 2024

Accepted: 19 August 2025

Published online: 2 October 2025

 Check for updates

Nadav Auerbach^{1,6}, Surajit Dutta^{1,6}, Matan Uzan^{1,6}, Yaar Vituri¹, Yaozhang Zhou¹, Alexander Y. Meltzer¹, Sameer Grover¹, Tobias Holder², Peleg Emanuel¹, Martin E. Huber³, Yuri Myasoedov¹, Kenji Watanabe⁴, Takashi Taniguchi⁵, Yuval Oreg¹, Erez Berg¹ & Eli Zeldov¹✉

The tunable band structure and non-trivial topology of multilayer rhombohedral graphene lead to a variety of correlated electronic states with isospin orders—meaning ordered states in the combined spin and valley degrees of freedom—dictated by the interplay of spin–orbit coupling and Hund’s exchange interactions. However, methods for mapping local isospin textures and determining the exchange energies are currently lacking. Here we image the magnetization textures in tetralayer rhombohedral graphene using a nanoscale superconducting quantum interference device. We observe sharp magnetic phase transitions that indicate spontaneous time-reversal symmetry breaking. In the quarter-metal phase, the spin and orbital moments align closely, providing a bound on the spin–orbit-coupling energy. We also show that the half-metal phase has a very small magnetic anisotropy, which provides an experimental lower bound on the intervalley Hund’s exchange interaction energy. This is found to be close to its theoretical upper bound. The ability to resolve the local isospin texture and the different interaction energies will allow a better understanding of the phase transition hierarchy and the numerous correlated electronic states arising from spontaneous and induced isospin symmetry breaking in graphene heterostructures.

Magnetism has been studied since antiquity, yet understanding how magnetic order emerges in complex, interacting systems remains a challenge. In solids, magnetism generally stems from electron spin or orbital motion. Although spin moments dominate in most materials, recent studies on two-dimensional (2D) van der Waals systems reveal a leading role for orbital magnetism. Unlike spin-based magnetism, orbital magnetism reflects the distribution of electron wavefunctions and encodes the band topology and Berry curvature. In addition to spin,

electrons in graphene-like 2D materials exhibit a valley degree of freedom, which strongly influences their behaviour. Crucially, spontaneous magnetization is forbidden if time-reversal or full spin-valley isospin symmetry is preserved. Thus, magnetism in these systems offers key insights into symmetry breaking and electronic interactions in strongly interacting 2D materials^{1–3}.

An important characteristic of atomic-layer materials is their highly tunable electronic structure, which, together with a high

¹Department of Condensed Matter Physics, Weizmann Institute of Science, Rehovot, Israel. ²School of Physics and Astronomy, Tel Aviv University, Tel Aviv, Israel. ³Departments of Physics and Electrical Engineering, University of Colorado Denver, Denver, CO, USA. ⁴Research Center for Electronic and Optical Materials, National Institute for Materials Science, Tsukuba, Japan. ⁵Research Center for Materials Nanoarchitectonics, National Institute for Materials Science, Tsukuba, Japan. ⁶These authors contributed equally: Nadav Auerbach, Surajit Dutta, Matan Uzan. ✉e-mail: eli.zeldov@weizmann.ac.il

density of states (DOS) and non-trivial band geometry, can drive spontaneous symmetry breaking and the formation of magnetic ground states even at zero magnetic field^{4–8}. The resulting isospin symmetry breaking produces a rich array of textures, including spin and valley polarization, intervalley coherence (IVC), spin-valley locking via spin–orbit coupling (SOC), and skyrmion-like patterns^{9–14}. Rhombohedral multilayer graphene (RMG) has recently emerged as a low-disorder platform for realizing such a phase^{15–30}, including correlated insulators^{16,21,23,31}, Chern insulators^{31,32}, ferromagnets^{16,19,22,24,28–36}, ferroelectrics¹⁹, superconductors^{25,33,37–43} and multiferroics²⁸. Furthermore, proximity-induced SOC can stabilize certain phases^{34,35,37–43}, whereas moiré engineering enables exotic fractional quantum states^{24,29,30,32,44,45}.

In the absence of interactions, electronic bands with different valley and spin polarizations are degenerate. A key factor determining the energetic hierarchy of isospin symmetry-broken states is the Hund's exchange interaction, which describes interactions between electrons in the different isospin bands, comprising intravalley and intervalley components. Although intravalley exchange between opposite spins is usually the dominant energy due to the long-range nature of Coulomb interactions, intervalley exchange crucially shapes the material's low-energy physics. For example, in the absence of SOC, intervalley Hund's coupling favours a spin-ferromagnetic state over spin-antiferromagnetic states. SOC, by contrast, tends to stabilize intervalley spin-antiferromagnetic order in the absence of Hund's coupling. Thus, observing ferromagnetism indicates dominant intervalley Hund's interaction. It also permits spin-ferromagnetic IVC (a charge density wave), in contrast to antiferromagnetic IVC (a spin density wave). Despite its fundamental importance, a direct measurement of the Hund's interaction energy U_{Hu} has been lacking. In RMG, U_{Hu} is believed to be ferromagnetic, but directly probing its strength is challenging because it requires a perturbation that couples oppositely to spins in different valleys—unavailable experimentally. However, intrinsic Ising SOC (λ_{SOC}) acts exactly as such a perturbation, generating a small spin anisotropy of the order of $\lambda_{\text{SOC}}^2/U_{\text{Hu}}$. By rotating a small external magnetic field, we probe this anisotropy, enabling a quantitative measurement of U_{Hu} .

Previous studies on isospin ordering in van der Waals materials have largely relied on global measurements and theoretical models^{22,24,28–32,34,35,39,42,46}. Here we introduce a nanoscale magnetic imaging technique to directly visualize local isospin textures in the symmetry-broken phases of crystalline ABCA graphene. We further explore how magnetic fields affect isospin state stability, particularly via interactions with Berry curvature and orbital magnetization. The field influences both spin moments through the Zeeman effect and orbital moments via a valley Zeeman effect, resulting in band shifts^{15,47}. Our results show that the combination of momentum-dependent Berry curvature and unique band structure induces non-trivial magnetic band reconstruction, establishing RMG as a versatile platform for exploring the interplay of topology and interaction-driven physics¹².

Transport and topological magnetic band reconstruction

Three dual-gated ABCA graphene devices were studied, showing qualitatively similar behaviour (Fig. 1 and Extended Data Figs. 1 and 5). The d.c. top- and bottom-gate voltages $V_{\text{tg}}^{\text{dc}}$ and $V_{\text{bg}}^{\text{dc}}$, respectively, control the carrier density n and out-of-plane displacement field D . Figure 1d presents the longitudinal resistance $R_{\text{xx}}(n, D)$ at zero out-of-plane magnetic field ($B_z = 0$) in device A, which displays metallic behaviour with $R_{\text{xx}} < 1 \text{ k}\Omega$ for $|n| \gtrsim 0.5 \times 10^{12} \text{ cm}^{-2}$. Several ridge-like features partition the phase diagram. We focus on the weak ridge, $n_a(D)$ (Fig. 1d, white dashed line), which traces a kink in the quantum oscillations (QOs) when B_z is raised to 3 T (Fig. 1e). To its left, vertical QOs reflect a simple band structure with a single Fermi surface (Fig. 1c, left inset) and

fourfold-degenerate Landau levels (LLs). Our single-particle band structure calculations (Extended Data Fig. 3) accurately reproduce both transition line $n_a(D)$ and QOs in regions A and B (Fig. 1f). The $n_a(D)$ line reflects a Lifshitz transition—annulus opening in the valence band—producing a sharp step in the DOS (Fig. 1c, black arrow). Since at $|n| > |n_a(D)|$, the band structure is simple and no substantial interaction effects are expected due to low DOS, no additional transitions at higher densities are anticipated, as confirmed at zero field (Fig. 1d). Unexpectedly, in this full metal (M) phase, the QOs exhibit a break along the $n_a(D)$ line (Fig. 1e, cyan dashed line), across which the QOs display a π shift. Such a shift has been observed previously in rhombohedral structures, but remains unexplained¹. The high-resolution measurement and low disorder allow resolving the π shift as splitting of fourfold LLs and their recombination with neighbouring LLs. As described in the Supplementary Information, this is a result of the topological magnetic band reconstruction (TMBR) due to large Berry-curvature-induced orbital magnetization \mathcal{M}_{SR} in the annular Fermi surface (Fig. 1a and Extended Data Fig. 2), which in the presence of B_z , gives rise to pronounced splitting in the DOS between the K and K' valleys (Fig. 1c) and in band distortion, $\varepsilon(k) = \varepsilon_0(k) - \mathcal{M}_{\text{SR}}(k)B_z$ (Fig. 1b).

Spontaneous symmetry breaking

The rich QOs in R_{xx} (Fig. 1e) reveal several symmetry-broken states. The vertical QO lines in region A correspond to fourfold-degenerate LLs in a full metal with a single Fermi surface. The annulus opening at $n_a(D)$ introduces two Fermi surfaces in region B, with LLs from each. The TMBR further lifts valley degeneracy, yielding a full metal with four sets of intersecting LLs (Extended Data Fig. 3). At lower $|n|$, interaction-driven isospin symmetry breaking emerges. Regions D and F exhibit vertical QOs like region A, but with periods $\Delta n = \frac{N\hbar}{eB_z}$,

corresponding to LL degeneracies of $N = 2$ and $N = 1$, revealing half-metal (1/2M) and quarter-metal (1/4M) phases, respectively, with simple Fermi surfaces (\hbar , Planck's constant; e , elementary charge; Extended Data Fig. 4).

Imaging isospin magnetism

To probe the nature of the symmetry-broken states, we performed nanoscale magnetic imaging on device B utilizing a superconducting quantum interference device (SQUID) on the apex of a sharp pipette (SQUID on tip (SOT))^{48,49}. A small a.c. voltage $V_{\text{tg}}^{\text{ac}}$ applied to the top gate modulates n by n_{ac} (Fig. 2d), inducing a differential change in the local magnetization $m(x, y)$ and corresponding stray field $B_z^{\text{ac}}(x, y)$, detected by the SOT. Figure 2a shows $B_z^{\text{ac}}(n, D)$ at a fixed location above the sample at low $B_z = 10 \text{ mT}$. Two sharp peak lines indicated an abrupt increase in magnetization \mathcal{M} at M-to-1/2M and 1/2M-to-1/4M phase transitions, consistent with the transport data (Extended Data Fig. 5). In a state that preserves time-reversal symmetry, the net magnetization vanishes. Time-reversal symmetry breaking induces magnetization via charge imbalance in spin or valley sectors. The 2D graphene structure dictates a highly anisotropic orbital magnetic moment (schematic of the current loops is shown in Fig. 2f–h) with an easy \hat{z} axis. By contrast, our understanding of spin anisotropy is lacking due to limited ability for direct experimental visualization of the spin properties. Contrary to orbital moment, spin anisotropy (Fig. 2f–h, spheres with arrows) is governed by the interplay between SOC and Hund's interactions¹⁸ and can, therefore, vary considerably between the different states. To investigate isospin anisotropy, we image $B_z^{\text{ac}}(x, y)$ as B_a is rotated.

Isospin anisotropy in 1/2M

Figure 3g shows $B_z^{\text{ac}}(x, y)$ measured in $B_z = 15 \text{ mT}$ ($B_x = 0 \text{ mT}$, $\tan\theta_B = B_x/B_z = 0$) across the M-to-1/2M phase transition. Using an inversion procedure (Methods), we reconstruct the local differential magnetization $m(x, y)$ (Fig. 3j). Since n_{ac} modulation induces a.c. switching between adjacent phases, the differential magnetization,

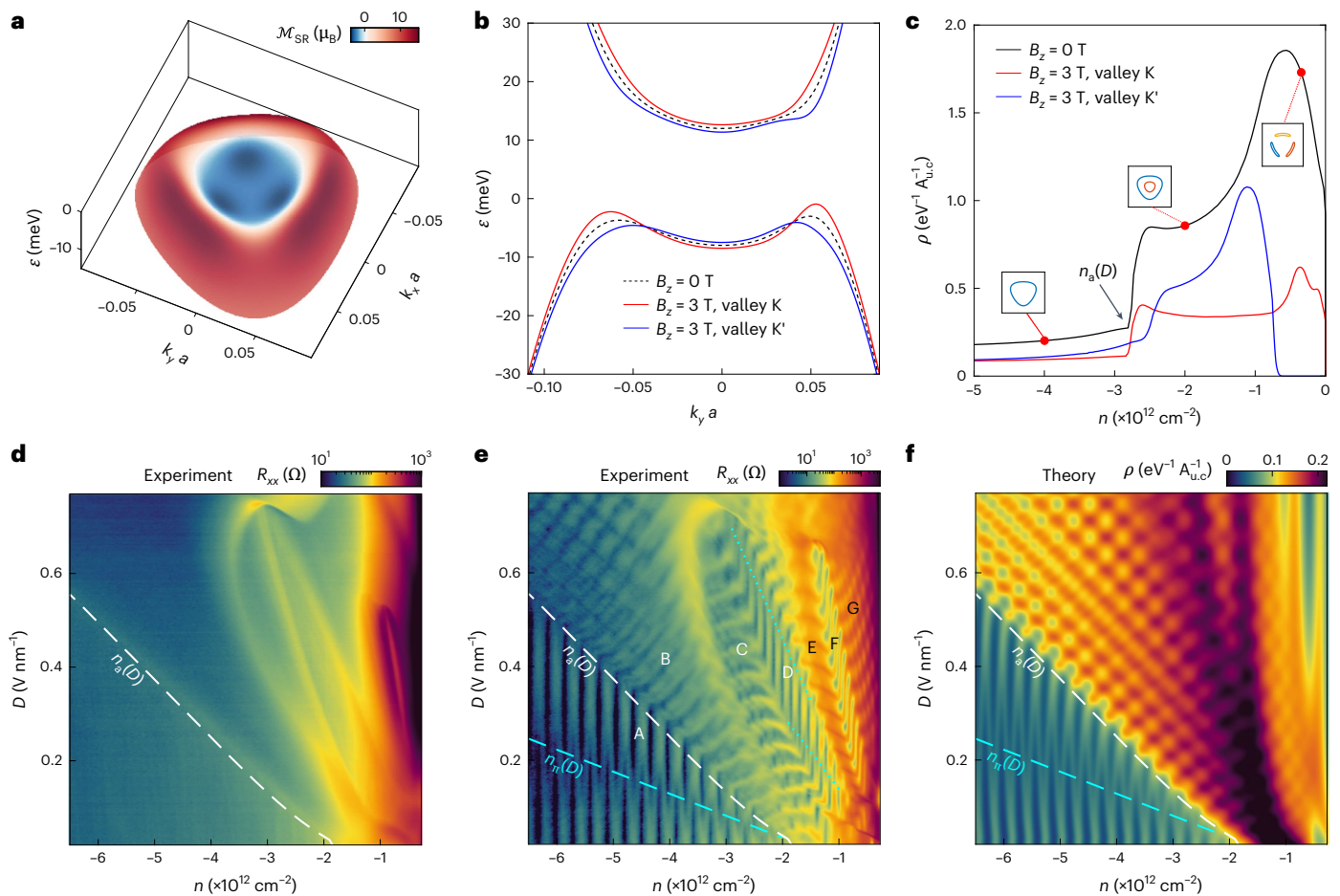


Fig. 1 | TMBR and transport measurements in ABCA graphene. **a**, Surface plot of the calculated low-energy band structure of the valence band $\varepsilon(k)$ with overlaid colour-coded self-rotation magnetization $\mathcal{M}_{SR}(k)$ of the K' valley for displacement potential $\Delta_1 = 10$ meV at $B_z = 0$ T (Supplementary Information). **b**, Energy dispersion, $\varepsilon(k) = \varepsilon_0(k) - \mathcal{M}_{SR}(k)B_z$, along $(0, k_y)$ for $\Delta_1 = 10$ meV at $B_z = 0$ T (dashed) and $B_z = 3$ T, resulting in TMBR and degeneracy lifting between K (red) and K' (blue) valleys. **c**, Corresponding valence band DOS, ρ , versus n without (black) and with valley degeneracy lifting by TMBR for K (red) and K' (blue) valleys. A full valley polarization occurs at $|n| < 0.76 \times 10^{12} \text{ cm}^{-2}$ at $B_z = 3$ T. The insets show the Fermi surface structure at the red points and the black arrow indicates the sharp step in DOS at annulus opening $n_a(D)$. **d**, Longitudinal resistance $R_{xx}(n, D)$ of device A at $B_z = 0$ T at $T = 500$ mK. The white dashed line is the theoretical fit of the Lifshitz transition $n_a(D)$. **e**, Same data as **d**, but for $B_z = 3$ T, showing different patterns of QOs in the various labelled regions. Region A, full

metal with single Fermi surface (s-M); region B, a-M with annular Fermi surface and partial TMBR-induced valley polarization; region C, full metal with spontaneous partial spin polarization and TMBR-induced valley polarization; region D, valley-degenerate spin-polarized 1/2M with single Fermi surface (s-1/2M); region E, a-1/2M with annular Fermi surface and possible partial valley polarization; region F, 1/4M with single Fermi surface; region G, 1/4M with annular Fermi surface. The cyan dashed curve in region A is the π -shift $n_\pi(D)$ line in full metal derived from the TMBR calculations with no fitting parameters. The cyan dotted curves in region D mark equivalent π -shift lines in the 1/2M phase. **f**, Calculated DOS showing oscillations due to LLs at $B_z = 3$ T in the presence of TMBR. The single-particle DOS effectively reproduces the QOs in regions A and B in **e**, where interaction effects are negligible ($D = 1$ V nm $^{-1}$ corresponds to $\Delta_1 = 97$ meV).

$\mathbf{m} = \mathcal{M}_{1/2M} - \mathcal{M}_M$, reflects the difference in local magnetization between the 1/2M and M phases (for clarity, the differential m is normalized by n in units of μ_B/e). Since the M phase has no magnetization, the measured m reflects the magnetization of the 1/2M phase.

Next, applying $B_z = 15$ mT rotates the field to $\theta_b = 45^\circ$, with the resulting $B_z^{ac}(x, y)$ shown in Fig. 3h. Although the overall $B_z^{ac}(x, y)$ looks similar, the stray field along the inner right edge is enhanced (red) and the outer edge field vanishes (green), rather than being negative (blue), as shown in Fig. 3g. By contrast, on the left edge, the outer field becomes more negative and the inner field is reduced. Additionally, bubble domains with suppressed B_z^{ac} become more oval and shift rightwards. For $\theta_b = -45^\circ$, similar effects but with a reversed orientation appear (Fig. 3i). These changes are consistent with the calculated stray fields for a uniform sample with tilted magnetization (Fig. 3b,c,e,f).

The data show that the isospin orientation in the 1/2M phase depends on the direction of B_a (Fig. 2g). To quantify the magnetization angle, we begin with the reconstructed $\mathbf{m}(x, y) = m(x, y) \hat{z}$

at $\theta_b = 0$ (Fig. 3j), rotate it by an angle θ_s such that $\mathbf{m}(x, y) = m(x, y) (\cos \theta_s \hat{z} + \sin \theta_s \hat{x})$, and compute the resulting $B_z^{ac}(x, y)$. The actual isospin magnetization angle θ_s is then extracted by best fitting the calculated and measured $B_z^{ac}(x, y)$ (Extended Data Fig. 8). The calculated $B_z^{ac}(x, y)$ (Fig. 3k) effectively reproduces the measured one (Fig. 3h), including the negative B_z^{ac} along the left edge, the enhanced field at the right edge and bubble distortions. A similarly accurate fit for $\theta_b = -45^\circ$ is shown in Fig. 3l. This approach enables the extraction of both magnitude and orientation of the isospin magnetic moment (Methods).

Figure 4f shows θ_s versus θ_b , revealing that in the 1/2M phase, isospin magnetism is nearly isotropic and aligns closely with B_a . Given the strong \hat{z} -axis anisotropy of orbital magnetism, this confirms that 1/2M in tetralayer rhombohedral graphene is a valley-degenerate, spin-polarized ferromagnet, consistent with prior RMG studies^{21,24,31}. However, full spin isotropy in the presence of SOC implies a large inter-valley Hund's coupling, as discussed below.

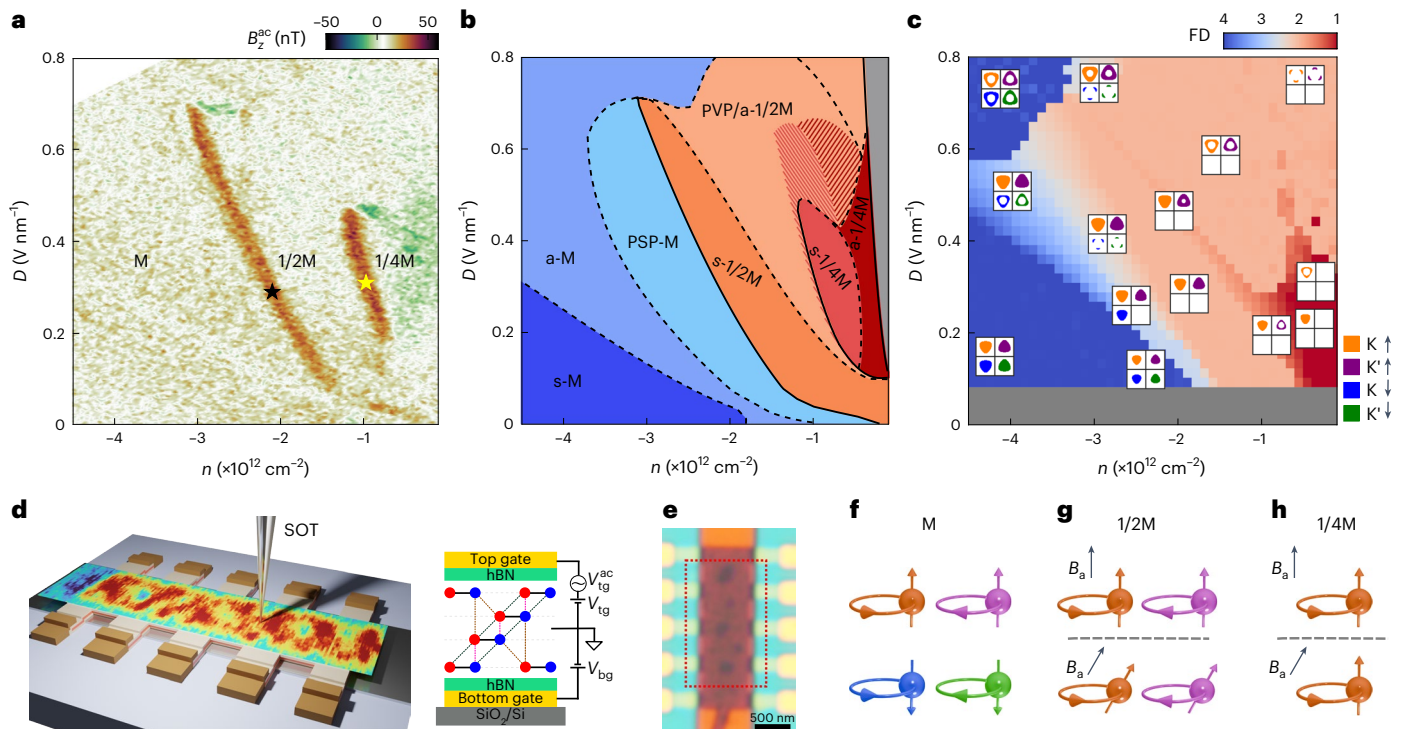


Fig. 2 | Symmetry-broken isospin phase diagram in ABCA graphene. **a**, $B_z^{ac}(n, D)$ measured in the bulk of the sample at $T = 20$ mK and $B_z = 10$ mT, showing a sharp differential magnetic signal along the M-to-1/2M and 1/2M-to-1/4M phase transition lines. **b**, Schematic of the experimentally derived phase diagram with labelled states. s-M, fourfold-degenerate full metal with a simple Fermi surface; a-M, full metal with an annular Fermi surface; PSP-M, partially spin polarized metal with TMBR-induced valley polarization; s-1/2M, twofold-degenerate fully spin polarized 1/2M with a simple Fermi surface; PVP-1/2M, partially valley polarized annular 1/2M; s-1/4M, onefold-degenerate simple 1/4M; a-1/4M, annular 1/4M. Solid lines indicate sharp magnetic transitions and dashed lines represent continuous transitions. The red–orange striped regions schematically show the expansion of the s-1/4M and a-1/4M phases on increasing B_z (Extended Data Figs. 5 and 6). **c**, Calculated schF phase diagram, with the colour bar indicating FD. The squares show the corresponding derived ground-state fermiology, with the

coloured areas representing hole-occupied states of the four flavours. In the grey area, at low D , the numerical calculations are unreliable due to the overlap of conduction and valence bands. **d**, Schematic of the sample layout with scanning SOT revealing the local magnetization pattern (left). Schematic of the cross-section of the encapsulated ABCA graphene with the electrical diagram (right). **e**, Optical image of the ABCA graphene device B patterned into Hall bar geometry, with the scan window indicated by the red dotted rectangle. The dark circular patches in the central region are bubbles. **f–h**, Isospin schematics with orbital (circular trajectories) and spin (balls with arrows) sectors. **f**, Fourfold-degenerate metal with zero magnetization. **g**, Twofold valley-degenerate spin-polarized 1/2M in out-of-plane (top) and tilted (bottom) B_a , with isotropic magnetization and spin direction following the B_a orientation. **h**, Onefold spin- and valley-polarized 1/4M in out-of-plane (top) and tilted (bottom) B_a . The isospin magnetization is highly anisotropic with easy \hat{z} axis and spin locked to the orbital moment.

For B_a along \hat{z} ($\theta_b = 0$), the symmetric negative stray field B_z^{ac} outside the right and left edges (Fig. 3g) is symmetric, which matches the calculations for $m(x, y)$ aligned along \hat{z} (Fig. 3a,d and Methods). The reconstructed $m(x, y)$ is rather uniform in the sample bulk (Fig. 3g,j, red–yellow), except for circular patches (blue) in which the magnetization vanishes. These are the bubbles formed during fabrication (Fig. 2e), which induce strain and disorder that destroy the symmetry-broken phases, as seen in magic-angle bilayer graphene⁵⁰.

Anisotropy in 1/4M

Figure 2a reveals a sharp peak in differential magnetization at the 1/2M-to-1/4M transition, indicating greater magnetization in the 1/4M phase. Since 1/2M is already spin polarized, this increase must stem from additional valley polarization. To probe the isospin structure, we image $B_z^{ac}(x, y)$ across the transition. Figure 4a shows the data at $\theta_b = 0^\circ$, with the reconstructed $m(x, y)$ shown in Fig. 4d. The $m(x, y)$ pattern resembles that of the M-to-1/2M transition, but with over threefold-higher amplitude, exceeding $1 \mu_B/e$. Since for $\theta_b = 0^\circ$, the spin is aligned along \hat{z} with the same contribution to magnetization in both 1/2M and 1/4M phases, the observed differential $m(x, y)$ across the transition reflects only the Berry-curvature-induced orbital magnetization in 1/4M, emphasizing its dominant contribution.

Rotating B_a to $\theta_b = 83^\circ$, the resulting $B_z^{ac}(x, y)$ in Fig. 4b shows the negative stray field shifting to the right edge—opposite to its position

in Fig. 3e,h—suggesting that the differential magnetization behaves as if tilted to negative θ_s (Fig. 3f,i). This counterintuitive behaviour reveals a strong SOC in the 1/4M phase, aligning both spin and orbital moments along \hat{z} . As a result, the difference between the out-of-plane magnetization in 1/4M and the $\theta_s = 83^\circ$ spin tilt in 1/2M results in differential magnetization that appears to a negative θ_s . Similarly, for $\theta_b = -83^\circ$, the differential magnetization appears to be oriented in the positive direction with negative B_z^{ac} on the left edge (Fig. 4c). As discussed in the Methods, we can qualitatively reproduce the measured $B_z^{ac}(x, y)$ in Fig. 4b by the proper superposition of orbital and spin-tilted $m(x, y)$ patterns from Figs. 4d and 3j, as shown in Fig. 4e. These observations show that, unlike the nearly isotropic 1/2M phase, the 1/4M phase exhibits strong isospin anisotropy with an easy \hat{z} axis (Fig. 4f (magenta triangles) and Extended Data Fig. 9).

Analysis of isospin anisotropy and Hund's and SOC energies

The stark anisotropy difference between the 1/2M and 1/4M phases can be qualitatively understood as follows. In 1/4M, the spin anisotropy is dictated by SOC energy λ_{SOC} , which tends to align the spin and valley moments. Considering SOC and Zeeman effects under tilted fields, the spin tilt angle is given by $\tan \theta_s = \frac{B_x}{B_z + \lambda_{\text{SOC}}/(g\mu_B)}$ (Methods), with g being the gyromagnetic ratio. The three rightmost curves in Fig. 4f

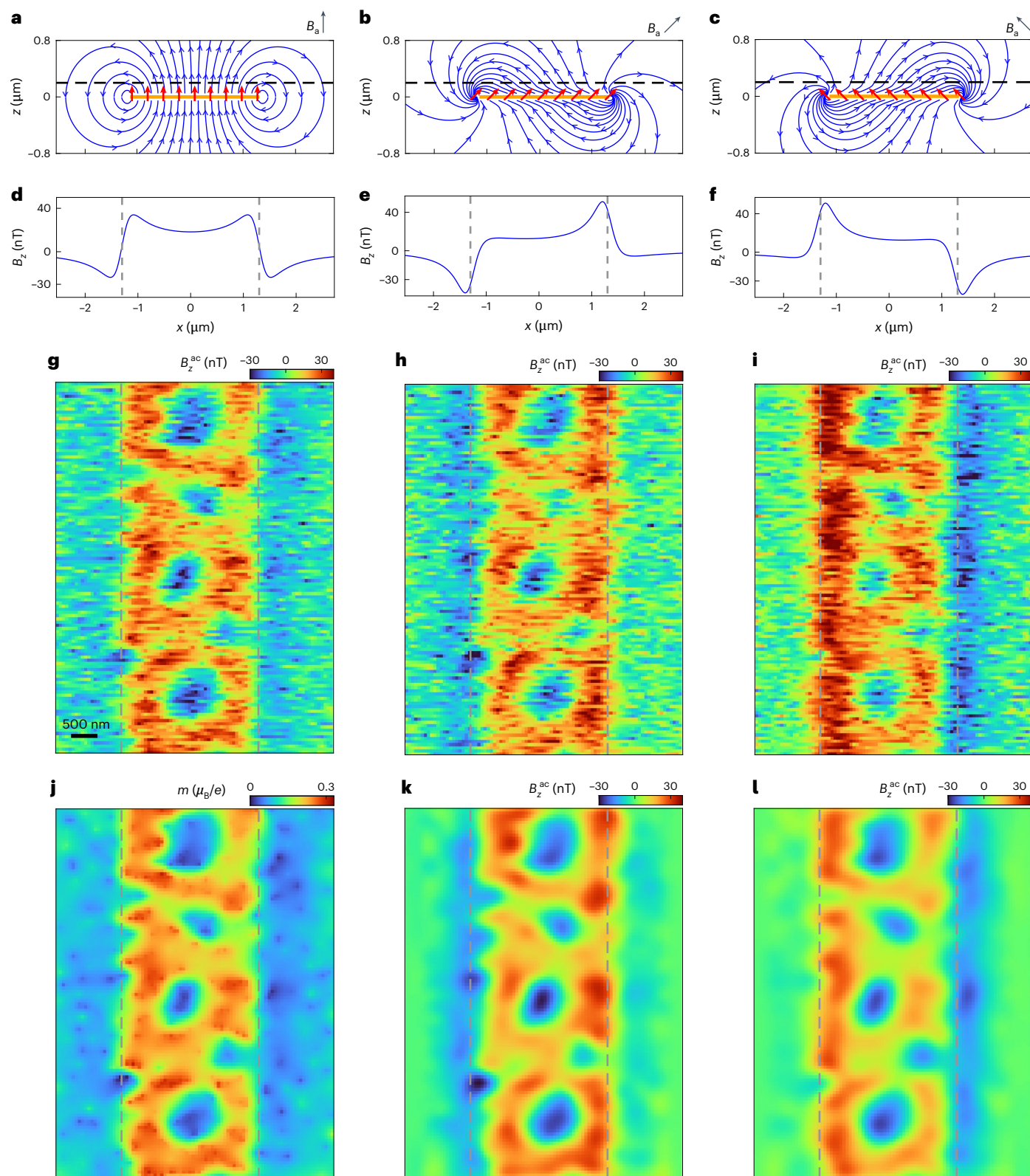


Fig. 3 | Isospin texture in the 1/2M phase. **a**, Schematic of the cross-section of graphene (orange) with isospin magnetic moments (red) oriented along \hat{z} ($\theta_s = 0$) with the corresponding calculated stray magnetic field lines. **b, c**, Same data as **a**, but for isospins tilted at $\theta_s = 45^\circ$ (**b**) and $\theta_s = -45^\circ$ (**c**). **d**, Calculated out-of-plane stray magnetic field $B_z(x)$ at a height of 200 nm above graphene (dashed line in **a**) for uniform magnetization of $0.63 \times 10^{12} \mu_B \text{ cm}^{-2}$. The vertical dotted lines correspond to graphene edges. **e**, Same data as **d**, but for $\theta_s = 45^\circ$. The positive B_z peak resides on the inner side of the right graphene edge, whereas the negative peak resides on the outer side of the left edge. **f**, Same data as **e**, but for $\theta_s = -45^\circ$.

g, Measured out-of-plane stray field $B_z^{ac}(x, y)$ at the M-to-1/2M transition (black star in Fig. 2a) for B_a at $\theta_b = 0$. The blue circular regions correspond to the locations of the bubbles (Fig. 2e). **h**, Same data as **g**, but for $\theta_b = 45^\circ$. The negative B_z^{ac} is enhanced outside the left edge, whereas the positive B_z^{ac} is enhanced on the inner side of the right edge. **i**, Same data as **h**, but for $\theta_b = -45^\circ$. **j**, Local differential magnetization $m(x, y)$ reconstructed from **g**. **k**, Calculated $B_z^{ac}(x, y)$ from $m(x, y)$ in **j** tilted to $\theta_s = 45^\circ$, reproducing the measured $B_z^{ac}(x, y)$ in **h**. **l**, Same data as **k**, but for $\theta_s = -45^\circ$.

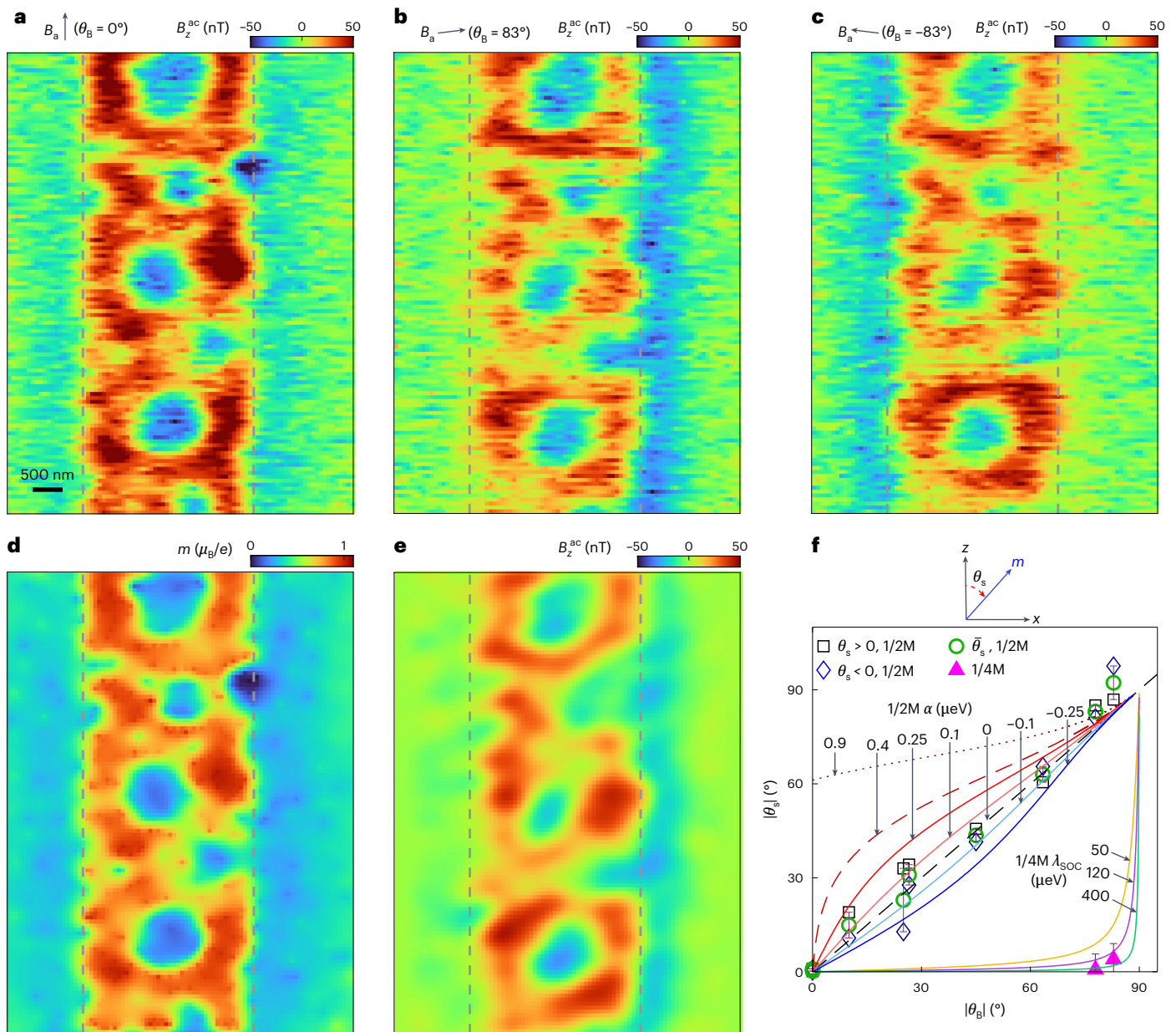


Fig. 4 | Isospin texture in the 1/4M phase. a, Measured $B_z^{ac}(x, y)$ at the 1/2M-to-1/4M transition (yellow star in Fig. 2a) for B_s along $\theta_B = 0$. **b**, Same data as **a**, but for $\theta_B = 83^\circ$. In contrast to Fig. 3h, the negative B_z^{ac} occurs at the right graphene edge due to spin tilting in the 1/2M phase. **c**, Same data as **b**, but for $\theta_B = -83^\circ$. **d**, Local differential magnetization $m(x, y)$ reconstructed from **a**. **e**, $B_z^{ac}(x, y)$ calculated using a superposition of the orbital $m(x, y)$ in the 1/4M shown in **d** and of a tilted spin $m(x, y)$ in the 1/2M phase based on Fig. 3j, qualitatively reproducing the measured $B_z^{ac}(x, y)$ in **b**. **f**, Derived spin tilt angle $|\theta_s|$ versus the applied field tilt angle $|\theta_B|$ for positive (black squares) and negative (blue diamonds) angles across the M-to-1/2M and 1/2M-to-1/4M (solid magenta triangles) transitions. The magenta error bars at 1/2M-to-1/4M transitions are estimated by comparing B_z^{ac} for $|\theta_B| = 78^\circ$ and $|\theta_B| = 83^\circ$ (Methods). The green

open circles represent the average spin tilt angle, $\bar{\theta}_s = (|\theta_s(>0)| + |\theta_s(<0)|)/2$, and the corresponding black error bars are defined as $(|\theta_s(>0)| - |\theta_s(<0)|)$. The solid lines show the calculated θ_s versus θ_B (Methods) for various indicated values of λ_{SOC} in 1/4M and α in 1/2M for $B_z = 15 \text{ mT}$ and variable $B_x = B_s \tan \theta_B$. The 1/4M lines set a lower bound on Ising SOC of $\lambda_{SOC} \gtrsim 120 \mu\text{eV}$, substantially higher than the previously evaluated $\lambda_{SOC} = 50 \mu\text{eV}$ (yellow curve) in ABC graphene¹⁸. The magnetism in the 1/2M phase is essentially fully isotropic with the calculated solid lines setting an upper bound on spin anisotropy of $|\alpha| < 0.25 \mu\text{eV}$, which sets a lower bound on $U_{Hu} \gtrsim 6.5 \text{ meV}$ (Methods). The red dashed line shows the calculated θ_s versus θ_B for $\alpha = 0.4 \mu\text{eV}$ based on previously assumed $U_{Hu} = 4.2 \text{ meV}$ (refs. 41,51), which is inconsistent with the data.

show the calculated θ_s versus $\theta_B = \tan^{-1}(B_x/B_z)$ for different values of λ_{SOC} at $B_z = 15 \text{ mT}$ and variable B_x , which allows us to set a lower bound on Ising $\lambda_{SOC} \gtrsim 120 \mu\text{eV}$. This experimental estimate of the SOC strength in ABCA is more than twice the previously evaluated $\lambda_{SOC} = 50 \mu\text{eV}$ in ABC graphene¹⁸.

The extracted λ_{SOC} raises a question regarding the isotropic spin moment measured in the 1/2M phase. A finite SOC means that full spin rotation is not a symmetry of the system, and hence, we expect the spin

ferromagnetic phase to be anisotropic (either easy axis or easy plane). However, the spin anisotropy α in 1/2M is strongly suppressed by Hund's coupling $\alpha \cong \lambda_{SOC}^2/8U_{Hu}$, where $U_{Hu} = \eta J_H$ is the intervalley Hund's coupling energy (Methods). Therefore, to explain the seemingly isotropic spin moment, U_{Hu} should be sufficiently large. The 1/2M phase (Fig. 4f, solid lines) shows the calculated θ_s versus θ_B dependence for various values of α (Extended Data Fig. 7), from which we can set an upper bound on $|\alpha| < 0.25 \mu\text{eV}$. Using the attained $\lambda_{SOC} > 120 \mu\text{eV}$, this α value

leads to a lower bound on the Hund's coupling of $U_{\text{Hu}} > 6.5 \text{ meV} = 75.4 \text{ K}$, and of the corresponding $J_{\text{H}} > 3.1 \times 10^{-12} \text{ meV cm}^2$. This measurement of the Hund's-type intervalley exchange energy is substantially larger than the values of $J_{\text{H}} \cong 2 \times 10^{-12} \text{ meV cm}^2$ previously used in the literature for modelling rhombohedral graphene^{18,41,51}. Such a large Hund's energy scale means that relative spin fluctuations between the two valleys are suppressed. For temperatures below this energy scale, the total spin moment for the two valleys should be treated as a single degree of freedom, whereas at higher temperatures, the spin moments associated with each valley should be considered as independent degrees of freedom.

Phase diagram

Low-field magnetization data (Fig. 2a) reveal three main phases—M, 1/2M and 1/4M—separated by sharp phase transitions. Examination of the QOs at high magnetic fields (Fig. 1e and Extended Data Fig. 4), by contrast, discloses additional symmetry-broken states within the main phases (Fig. 2b). The M phase, in which all four flavours are occupied, is subdivided into three states: simple s-M with a single Fermi surface, a-M with an annular Fermi surface, and spontaneously symmetry-broken partially spin-polarized PSP-M phase. Since the partially spin-polarized state is partially polarized, the sharp transition from PSP-M to fully spin-polarized 1/2M should be accompanied by a reduced jump in magnetization, in accordance with the observed $m \cong 0.3 \mu_{\text{B}}/e$ at the M-to-1/2M transition. The 1/2M phase is subdivided into valley-symmetric s-1/2M with a simple Fermi surface and a-1/2M with an annular Fermi surface, which is possibly also a partially valley-polarized PVP-1/2M phase. Note that similar to full metal, the TMBR-induced π shifts are also observed in s-1/2M (Fig. 1e, cyan dotted lines), revealing magnetic-field-induced partial valley polarization. Finally, the 1/4M phase is also subdivided into a single Fermi surface (s-1/4M) and annular (a-1/4M) states. Since 1/4M comprises only one valley and one spin, no π shifts should occur. In particular, the 1/4M region expands markedly with the field (Fig. 2b, striped regions), as observed by comparing Fig. 1d,e and described in Extended Data Fig. 6. This expansion is a result of the magnetic energy gain due to orbital magnetic moment in 1/4M, which is absent in the adjacent 1/2M phase (Supplementary Information). These conclusions are corroborated by self-consistent Hartree–Fock (scHF) calculations with a gate-screened Coulomb interaction (Supplementary Information). Figure 2c shows the derived phase diagram with colour-coded flavour degeneracy: $\text{FD} = n/\max(n_i)$, where n_i is the carrier density in each isospin flavour, showing a sequence of symmetry-breaking transitions from M to 1/4M, which broadly agrees with the measured diagram in Fig. 2b.

Discussion

A comparison of isospin transitions in ABCA and ABC graphene¹⁸ shows that in both systems, full spin polarization does not occur immediately. Instead, there is a gradual polarization, too weak to be detected locally, followed by an abrupt transition to a fully spin-polarized 1/2M phase. Similarly, in the presence of a magnetic field, the spin-polarized 1/2M phase apparently undergoes gradual valley polarization, before an abrupt transition to a 1/4M phase. In particular, although ABC graphene exhibits IVC ordering within 1/4M, ABCA shows no such signatures, either in measurements or scHF simulations. This is particularly interesting since hole-doped ABC graphene has been found to become superconducting at subkelvin temperatures²⁵, whereas, so far, no superconducting phase has been reported in a pure hole-doped tetralayer⁴³. The ABCA phase diagram, thus, presents a valuable comparison for narrowing down the superconducting mechanism. Importantly, the hole-doped ABCA seems to be lacking IVC phases and its superconductivity is apparently suppressed, whereas in ABC, both phases are present, which is consistent with recent suggestions of a pairing mechanism mediated by IVC fluctuations^{10,11,14,27}. Since our findings clearly indicate that the isospin anisotropy throughout the phase diagram

depends subtly on small differences in microscopic properties, a better understanding of the underlying electronic correlations is necessary.

The findings not only shed light on the microscopic aspects of isospin ordering in fine detail but also demonstrate that RMG is a highly tunable and increasingly well-understood system with superior device quality compared with twisted stackings. Recent work on spin–orbit-proximitized RMG has uncovered superconducting phases absent without a strong SOC^{37–42}, potentially originating from a spin-canted in-plane ferromagnetic state^{17,41}. Our experimental estimate of Hund's coupling is crucial for a quantitative understanding of spin-canted ferromagnetism and possibly related superconducting phases. We conclude that screening effects on the Hund's coupling are weak, as the attained $U_{\text{Hu}} > 6.5 \text{ meV}$ is suppressed by less than a factor of two relative to the maximum value of intervalley Coulomb energy in a vacuum (Methods). Comparable Hund's coupling is, thus, expected across different rhombohedral graphene systems.

Online content

Any methods, additional references, Nature Portfolio reporting summaries, source data, extended data, supplementary information, acknowledgements, peer review information; details of author contributions and competing interests; and statements of data and code availability are available at <https://doi.org/10.1038/s41567-025-03035-z>.

References

- Pantaleón, P. A. et al. Superconductivity and correlated phases in non-twisted bilayer and trilayer graphene. *Nat. Rev. Phys.* **5**, 304–315 (2023).
- Burgos Atencia, R., Agarwal, A. & Culcer, D. Orbital angular momentum of Bloch electrons: equilibrium formulation, magneto-electric phenomena, and the orbital Hall effect. *Adv. Phys. X* **9**, 2371972 (2024).
- Xiao, D., Chang, M.-C. & Niu, Q. Berry phase effects on electronic properties. *Rev. Mod. Phys.* **82**, 1959–2007 (2010).
- Zhang, F., Jung, J., Fiete, G. A., Niu, Q. & MacDonald, A. H. Spontaneous quantum Hall states in chirally stacked few-layer graphene systems. *Phys. Rev. Lett.* **106**, 156801 (2011).
- Lu, X. et al. Superconductors, orbital magnets and correlated states in magic-angle bilayer graphene. *Nature* **574**, 653–657 (2019).
- Sharpe, A. L. et al. Emergent ferromagnetism near three-quarters filling in twisted bilayer graphene. *Science* **365**, 605–608 (2019).
- Tschirhart, C. L. et al. Imaging orbital ferromagnetism in a moiré Chern insulator. *Science* **372**, 1323–1327 (2021).
- Grover, S. et al. Chern mosaic and Berry-curvature magnetism in magic-angle graphene. *Nat. Phys.* **18**, 885–892 (2022).
- Lee, Y. et al. Competition between spontaneous symmetry breaking and single-particle gaps in trilayer graphene. *Nat. Commun.* **5**, 5656 (2014).
- Chatterjee, S., Wang, T., Berg, E. & Zaletel, M. P. Inter-valley coherent order and isospin fluctuation mediated superconductivity in rhombohedral trilayer graphene. *Nat. Commun.* **13**, 6013 (2022).
- Dong, Z., Levitov, L. & Chubukov, A. V. Superconductivity near spin and valley orders in graphene multilayers. *Phys. Rev. B* **108**, 134503 (2023).
- Ghazaryan, A., Holder, T., Berg, E. & Serbyn, M. Multilayer graphenes as a platform for interaction-driven physics and topological superconductivity. *Phys. Rev. B* **107**, 104502 (2023).
- Huang, C. et al. Spin and orbital metallic magnetism in rhombohedral trilayer graphene. *Phys. Rev. B* **107**, L121405 (2023).
- Vituri, Y., Xiao, J., Pareek, K., Holder, T. & Berg, E. Incommensurate intervalley coherent states in ABC graphene: Collective modes and superconductivity. *Phys. Rev. B* **111**, 075103 (2025).

15. Slizovskiy, S., McCann, E., Koshino, M. & Fal'ko, V. I. Films of rhombohedral graphite as two-dimensional topological semimetals. *Commun. Phys.* **2**, 164 (2019).
16. Shi, Y. et al. Electronic phase separation in multilayer rhombohedral graphite. *Nature* **584**, 210–214 (2020).
17. Dong, Z., Lantagne-Hurtubise, É. & Alicea, J. Superconductivity from spin-canting fluctuations in rhombohedral graphene. Preprint at <https://doi.org/10.48550/arXiv.2406.17036> (2024).
18. Arp, T. et al. Intervalley coherence and intrinsic spin-orbit coupling in rhombohedral trilayer graphene. *Nat. Phys.* **20**, 1413–1420 (2024).
19. Winterer, F. et al. Ferroelectric and spontaneous quantum Hall states in intrinsic rhombohedral trilayer graphene. *Nat. Phys.* **20**, 422–427 (2024).
20. Zhumagulov, Y., Kochan, D. & Fabian, J. Emergent correlated phases in rhombohedral trilayer graphene induced by proximity spin-orbit and exchange coupling. *Phys. Rev. Lett.* **132**, 186401 (2024).
21. Liu, K. et al. Spontaneous broken-symmetry insulator and metals in tetralayer rhombohedral graphene. *Nat. Nanotechnol.* **19**, 188–195 (2024).
22. Wang, S. et al. Chern insulator states with tunable Chern numbers in a graphene moiré superlattice. *Nano Lett.* **24**, 6838–6843 (2024).
23. Kerelsky, A. et al. Moiréless correlations in ABCA graphene. *Proc. Natl Acad. Sci. USA* **118**, e2017366118 (2021).
24. Zhou, H. et al. Half- and quarter-metals in rhombohedral trilayer graphene. *Nature* **598**, 429–433 (2021).
25. Zhou, H., Xie, T., Taniguchi, T., Watanabe, K. & Young, A. F. Superconductivity in rhombohedral trilayer graphene. *Nature* **598**, 434–438 (2021).
26. Chou, Y.-Z., Wu, F., Sau, J. D. & Das Sarma, S. Acoustic-phonon-mediated superconductivity in moiréless graphene multilayers. *Phys. Rev. B* **106**, 024507 (2022).
27. Dong, Z., Lee, P. A. & Levitov, L. S. Signatures of Cooper pair dynamics and quantum-critical superconductivity in tunable carrier bands. *Proc. Natl Acad. Sci. USA* **120**, e2305943120 (2023).
28. Han, T. et al. Orbital multiferroicity in pentalayer rhombohedral graphene. *Nature* **623**, 41–47 (2023).
29. Zhou, W. et al. Layer-polarized ferromagnetism in rhombohedral multilayer graphene. *Nat. Commun.* **15**, 2597 (2024).
30. Xie, J. et al. Tunable fractional Chern insulators in rhombohedral graphene superlattices. *Nat. Mater.* **24**, 1042–1048 (2025).
31. Han, T. et al. Correlated insulator and Chern insulators in pentalayer rhombohedral-stacked graphene. *Nat. Nanotechnol.* **19**, 181–187 (2024).
32. Lu, Z. et al. Fractional quantum anomalous Hall effect in multilayer graphene. *Nature* **626**, 759–764 (2024).
33. Zhou, H. et al. Isospin magnetism and spin-polarized superconductivity in Bernal bilayer graphene. *Science* **375**, 774–778 (2022).
34. Han, T. et al. Large quantum anomalous Hall effect in spin-orbit proximitized rhombohedral graphene. *Science* **384**, 647–651 (2024).
35. Sha, Y. et al. Observation of a Chern insulator in crystalline ABCA-tetralayer graphene with spin-orbit coupling. *Science* **384**, 414–419 (2024).
36. Seiler, A. M. et al. Quantum cascade of correlated phases in trigonally warped bilayer graphene. *Nature* **608**, 298–302 (2022).
37. Holleis, L. et al. Nematicity and orbital depairing in superconducting Bernal bilayer graphene. *Nat. Phys.* **21**, 444–450 (2025).
38. Zhang, Y. et al. Enhanced superconductivity in spin-orbit proximitized bilayer graphene. *Nature* **613**, 268–273 (2023).
39. Choi, Y. et al. Superconductivity and quantized anomalous Hall effect in rhombohedral graphene. *Nature* **639**, 342–347 (2025).
40. Li, C. et al. Tunable superconductivity in electron- and hole-doped Bernal bilayer graphene. *Nature* **631**, 300–306 (2024).
41. Patterson, C. L. et al. Superconductivity and spin canting in spin-orbit-coupled trilayer graphene. *Nature* **641**, 632–638 (2025).
42. Yang, J. et al. Impact of spin-orbit coupling on superconductivity in rhombohedral graphene. *Nat. Mater.* **24**, 1058–1065 (2025).
43. Han, T. et al. Signatures of chiral superconductivity in rhombohedral graphene. *Nature* **643**, 654–661 (2025).
44. Yang, J. et al. Spectroscopy signatures of electron correlations in a trilayer graphene/hBN moiré superlattice. *Science* **375**, 1295–1299 (2022).
45. Bocarsly, M. et al. De Haas-van Alphen spectroscopy and magnetic breakdown in moiré graphene. *Science* **383**, 42–48 (2024).
46. de la Barrera, S. C. et al. Cascade of isospin phase transitions in Bernal-stacked bilayer graphene at zero magnetic field. *Nat. Phys.* **18**, 771–775 (2022).
47. Hwang, Y., Rhim, J.-W. & Yang, B.-J. Geometric characterization of anomalous Landau levels of isolated flat bands. *Nat. Commun.* **12**, 6433 (2021).
48. Finkler, A. et al. Self-aligned nanoscale SQUID on a tip. *Nano Lett.* **10**, 1046–1049 (2010).
49. Vasyukov, D. et al. A scanning superconducting quantum interference device with single electron spin sensitivity. *Nat. Nanotechnol.* **8**, 639–644 (2013).
50. Uri, A. et al. Mapping the twist-angle disorder and Landau levels in magic-angle graphene. *Nature* **581**, 47–52 (2020).
51. Koh, J. M., Alicea, J. & Lantagne-Hurtubise, É. Correlated phases in spin-orbit-coupled rhombohedral trilayer graphene. *Phys. Rev. B* **109**, 035113 (2024).

Publisher's note Springer Nature remains neutral with regard to jurisdictional claims in published maps and institutional affiliations.

Open Access This article is licensed under a Creative Commons Attribution 4.0 International License, which permits use, sharing, adaptation, distribution and reproduction in any medium or format, as long as you give appropriate credit to the original author(s) and the source, provide a link to the Creative Commons licence, and indicate if changes were made. The images or other third party material in this article are included in the article's Creative Commons licence, unless indicated otherwise in a credit line to the material. If material is not included in the article's Creative Commons licence and your intended use is not permitted by statutory regulation or exceeds the permitted use, you will need to obtain permission directly from the copyright holder. To view a copy of this licence, visit <http://creativecommons.org/licenses/by/4.0/>.

© The Author(s) 2025

Methods

Device fabrication

The hexagonal boron nitride (hBN)-encapsulated tetralayer graphene heterostructures were fabricated using the dry-transfer method. The hBN and graphene flakes were exfoliated onto a Si/SiO₂ (285 nm) substrate and picked up using a polycarbonate on a polydimethylsiloxane dome stamp. The number of layers of the graphene flakes was determined via optical contrast analysis against the Si substrate (using the G values in the RGB triplet) and further confirmed through step strength analysis in the dark-field mode. The stacking order of the graphene flakes was determined by the shape of the Raman 2D peak (Extended Data Fig. 1e), and its rhombohedral-stacked regions were isolated using high-power laser cutting. The Raman analysis was subsequently repeated on the final stack (Extended Data Fig. 1f) to rule out the possible relaxation of graphene to Bernal stacking.

To increase the yield of the rhombohedral structure, a single-pick strategy was used to avoid multiple pick-ups of graphene flakes during the stacking procedure, which enhanced relaxation to Bernal stacking. This involved pre-preparation of the lower part of the stack, comprising a backgate (annealed patterned metal or graphite stripe) covered with an hBN flake, followed by annealing at 500 °C under a vacuum. For the same reason, the graphene flake manipulations were done faster, at lower temperatures (<70 °C) than usual, and along the zigzag direction of graphene⁵². This modified stacking protocol can, in turn, encourage bubble formation (Fig. 2e). Unlike in other graphene stacks, the bubbles cannot be removed by thermal annealing or subsequent pick-ups since the graphene stacking configuration is susceptible to these procedures. The chirality of the edges (zigzag/armchair) was first determined from the dependence of the second-harmonic generation on the polarization angle in the hBN flakes^{53,54} and in Bernal-stacked trilayer region within the same flake as the tetralayer graphene of interest.

Subsequently, the top hBN and graphene flakes were transferred onto the pre-prepared bottom part. During these processes, the crystal axes (discerned from the straight edges) of the hBN and tetralayer graphene were intentionally misaligned using a mechanical rotation stage to avoid moiré correlations. A Ti (2 nm)/Au (10 nm) top gate was deposited onto the finalized stacks. Then, the devices were etched into a Hall bar geometry, and one-dimensional contacts were established through SF₆ and O₂ plasma etching, followed by Cr (4 nm)/Au (60–90 nm) evaporation. The Raman, second-harmonic generation measurements and laser cutting were performed using a WITec alpha300 R Raman imaging microscope using 532-nm and 1,064-nm wavelengths.

Device summary:

Devices A and C: Ti (2 nm)/Au (10 nm) top gate and graphite bottom gate. The top and bottom hBN thicknesses are -17 nm and -31 nm, respectively.

Device B: Ti (2 nm)/Au (10 nm) top gate and Ti (2 nm)/Pt (10 nm) bottom gate. The top and bottom hBN thicknesses are -18 nm and -29 nm, respectively.

SOT measurements

The local magnetic imaging was performed using a custom-built scanning SOT microscope in a dilution refrigerator. All the measurements were conducted at a nominal base temperature of $T = 20$ mK. For detecting the local magnetic fields, we used an indium SQUID fabricated on the tip of a pulled quartz pipette with an integrated shunt resistor⁵⁵. The effective diameter of the In SOT was 194 nm, with a field sensitivity down to 10 nT Hz^{-1/2} and operating fields up to 0.4 T. A cryogenic-series SQUID array amplifier was implemented to read-out the SOT signal^{56,57}. To control the scan height during imaging, the SOT was attached to a quartz tuning fork vibrating at a resonance frequency of around 32 kHz. A small a.c. voltage V_{tg}^{ac} was applied to the top gate with an amplitude of 100 mV to 200 mV (r.m.s.) and frequency of 0.7 kHz to 2 kHz, modulating the carrier density by n_{ac} and the corresponding a.c. change in the local magnetic field $B_z^{ac}(x, y)$ was acquired by the SOT.

All the presented $B_z^{ac}(x, y)$ images were measured on device B to avoid magnetic signals originating from the graphite bottom gate. Single-point measurements (like Fig. 2b) were recorded at a height of 70 nm above the surface of the top metal gate. The 2D spatial images (Figs. 3 and 4) were scanned at a constant height of about 150 nm above the top-gate surface, with a pixel size of 50 nm and integration time of 1.2 s per pixel. Figures 3g–i and 4a–c were acquired at (D, n) values of $(0.29 \text{ V nm}^{-1}, -2.1 \times 10^{12} \text{ cm}^{-2})$, $(0.31 \text{ V nm}^{-1}, 0.97 \times 10^{12} \text{ cm}^{-2})$ and $(0.31 \text{ V nm}^{-1}, 0.9 \times 10^{12} \text{ cm}^{-2})$, respectively.

The angle-dependent measurements were performed at fixed $B_z = 15$ mT or $B_z = 85$ mT and variable B_x . All the data points in Fig. 4f were acquired at $B_z = 15$ mT, except for $\theta_B < 30^\circ$ points, which were measured also at $B_z = 85$ mT.

Single-particle band structure calculations

To calculate the low-energy single-particle band structure of rhombohedral tetralayer graphene, we adopted the Slonczewski–Weiss–McClure parameterized tight-binding model¹². Using the sublattice states {A1, B1, A2, B2, A3, B3, A4, B4}, the low-energy Hamiltonian can be written as,

$$H_0 = \begin{bmatrix} \Delta_1 + \Delta_2 & v_0 \pi^\dagger & v_4 \pi^\dagger & v_3 \pi & 0 & \frac{1}{2} \gamma_2 & 0 & 0 \\ v_0 \pi & \Delta_1 + \Delta_2 + \delta & \gamma_1 & v_4 \pi^\dagger & 0 & 0 & 0 & 0 \\ v_4 \pi & \gamma_1 & \frac{\Delta_1}{3} - \Delta_2 + \delta & v_0 \pi^\dagger & v_4 \pi^\dagger & v_3 \pi & 0 & \frac{1}{2} \gamma_2 \\ v_3 \pi^\dagger & v_4 \pi & v_0 \pi & \frac{\Delta_1}{3} - \Delta_2 + \delta & \gamma_1 & v_4 \pi^\dagger & 0 & 0 \\ 0 & 0 & v_4 \pi & \gamma_1 & -\frac{\Delta_1}{3} - \Delta_2 + \delta & v_0 \pi^\dagger & v_4 \pi^\dagger & v_3 \pi \\ \frac{1}{2} \gamma_2 & 0 & v_3 \pi^\dagger & v_4 \pi & v_0 \pi & -\frac{\Delta_1}{3} - \Delta_2 + \delta & \gamma_1 & v_4 \pi^\dagger \\ 0 & 0 & 0 & 0 & v_4 \pi & \gamma_1 & -\Delta_1 + \Delta_2 + \delta & v_0 \pi^\dagger \\ 0 & 0 & \frac{1}{2} \gamma_2 & 0 & v_3 \pi^\dagger & v_4 \pi & v_0 \pi & -\Delta_1 + \Delta_2 \end{bmatrix}$$

where $\pi = \tau k_x + i k_y$, $v_i = \frac{\sqrt{3}}{2h} a_0 \gamma_i$ ($i = 0, 3, 4$) is the hopping velocity, τ is the valley index (+1 for K valley and -1 for K' valley) and $a_0 = 2.46 \text{ \AA}$ is the graphene lattice constant. The parameter δ corresponds to the on-site potential for the sublattices, which have the nearest neighbour on the adjacent layer. Δ determines the potential difference between the outer

layers and is approximately proportional to the applied displacement field D , and Δ_2 encodes the potential difference between the outer and middle layers. The hopping parameters were chosen by fitting the annulus opening line $n_a(D)$ in the full metal in Fig. 1d, which can be achieved with the same intra- and interlayer hopping values reported

previously for rhombohedral trilayer graphene²⁴, leading us to adjust only the value of the on-site energy Δ_2 compared with the trilayer. This results in the following values:

Parameter	γ_0	γ_1	γ_2	γ_3	γ_4	δ	Δ_2
Value (in eV)	3.1	0.38	-0.015	-0.29	-0.141	0.0105	0.002

From the fit to the π -shift line (Fig. 1), we find that the outer-layer potential difference $\Delta_1 = 97$ meV corresponds to the applied displacement field $D = 1$ V nm⁻¹.

Isospin anisotropy analysis and derivation of spin-orbit and Hund's coupling bounds

To understand the interplay between valley polarization and spin-moment anisotropy, we use a mean-field-inspired model assuming that isospin polarization is momentum independent, which allows us to parameterize the system as a density matrix, using two spinors (assuming no intervalley coherence):

$$\hat{\rho} = \frac{n_K}{n} |\Psi_K\rangle\langle\Psi_K| + \frac{n_{K'}}{n} |\Psi_{K'}\rangle\langle\Psi_{K'}| \quad (1)$$

$$|\Psi_K\rangle = a_1 |\uparrow K\rangle + a_2 |\downarrow K\rangle, \quad |\Psi_{K'}\rangle = a_3 |\uparrow K'\rangle + a_4 |\downarrow K'\rangle,$$

where $n = n_K + n_{K'}$, and both $|\Psi_K\rangle$ and $|\Psi_{K'}\rangle$ are normalized to 1. The energy per carrier is given by

$$E = \frac{1}{2} \chi_\tau^{-1} \langle \tau_z S_z \rangle - U_{\text{Hu}} \langle \bar{S}_+ \rangle \cdot \langle \bar{S}_- \rangle - \frac{\lambda_{\text{SOC}}}{2} \langle \tau_z S_z \rangle - \frac{g}{2} \mu_B \bar{B} \cdot \langle \bar{S} \rangle - \mu_v B_z \langle \tau_z \rangle, \quad (2)$$

where $\langle \bar{S}_\pm \rangle \equiv \frac{1}{2} \langle (1 \pm \tau_z) \bar{S} \rangle$ are valley-spin polarization vectors, χ_τ is the valley susceptibility, μ_v is the valley orbital magnetic moment, the spin and valley operators are taken to have eigenvalues of ± 1 , and we take $g = 2$ for the g -factor. The interaction energy $U_{\text{Hu}} = nJ_{\text{H}}$ is the Hund's coupling energy scale, determined by the carrier density times the intrinsic Hund's coupling, and we assume that it is ferromagnetic, as there is plenty of evidence that the 1/2M phase is a spin ferromagnet. The Ising SOC ($\frac{\lambda_{\text{SOC}}}{2} \langle \tau_z S_z \rangle$) can be related to a Kane-Mele-type SOC in monolayer graphene. In monolayer graphene, the Ising SOC vanishes due to either inversion or C_2 rotation symmetry and does not result in any observable spin anisotropy. However, as rhombohedral graphene under the displacement field breaks the inversion symmetry and does not have C_2 rotation symmetry to begin with, it develops a finite sublattice polarization, and the Kane-Mele-type SOC of the graphene monolayer translates to an Ising-type SOC with magnitude proportional to the amount of sublattice polarization of the Bloch wavefunctions. In general, for a fixed displacement field, the amount of sublattice polarization increases with the number of layers, as it is related to the potential difference between the top and bottom layers.

We use the following parameterization:

$$\hat{\rho} = \frac{1+\delta n}{2} |\Psi_K\rangle\langle\Psi_K| + \frac{1-\delta n}{2} |\Psi_{K'}\rangle\langle\Psi_{K'}|$$

$$|\Psi_K\rangle = (\cos \theta_- |\uparrow\rangle + \sin \theta_- |\downarrow\rangle) \otimes |K\rangle, \quad |\Psi_{K'}\rangle = (\cos \theta_+ |\uparrow\rangle + \sin \theta_+ |\downarrow\rangle) \otimes |K'\rangle, \quad (3)$$

where $\theta_\pm = \theta_s \pm \delta\theta$; therefore, we find

$$E = \frac{1}{2} \chi_\tau^{-1} (\delta n - \chi_\tau \mu_v B_z)^2 - U_{\text{Hu}} \frac{1-\delta n^2}{4} \cos(2\delta\theta) - \frac{\lambda_{\text{SOC}}}{2} (\sin \theta_s \sin \delta\theta + \delta n \cos \theta_s \cos \delta\theta) - \frac{g}{2} \mu_B [B_x (\sin \theta_s \cos \delta\theta - \delta n \cos \theta_s \sin \delta\theta) + B_z (\cos \theta_s \cos \delta\theta + \delta n \sin \theta_s \sin \delta\theta)]. \quad (4)$$

Physically, θ_s is the average spin angle, $\delta\theta$ is the relative spin-canting angle between the valleys, and δn is the relative valley density imbalance normalized by the total density (Extended Data Fig. 7). Assuming

λ_{SOC} to be a small energy scale relative to χ_τ^{-1} and U_{Hu} , we find the ground state to be 1/4M ($\langle \tau_z \rangle = \pm 1$) for $\chi_\tau^{-1} + \frac{U_{\text{Hu}}}{2} < 0$, and 1/2M ($\langle \tau_z \rangle = 0$) otherwise.

1/4M. As valley polarization breaks the time-reversal symmetry, in the 1/4M phase, there is an effective spontaneous magnetic field acting on the spin degree of freedom, originating from the SOC. We assume full valley polarization $\delta n = \pm 1$, and find

$$E_{\text{QM}} = -\frac{\lambda_{\text{SOC}}}{2} \langle \tau_z S_z \rangle - \frac{g}{2} \mu_B \bar{B} \cdot \langle \bar{S} \rangle = \mp \frac{\lambda_{\text{SOC}}}{2} \langle S_z \rangle - \frac{g}{2} \mu_B \bar{B} \cdot \langle \bar{S} \rangle. \quad (5)$$

The sign of valley polarization $\langle \tau_z \rangle = \delta n$ can be trained by an external field.

We derive the angle of spin moment from the z axis for a positive value of B_z :

$$\tan \theta_s = \frac{B_x}{B_z + \frac{\lambda_{\text{SOC}}}{g\mu_B}}. \quad (6)$$

Figure 4f shows the calculated θ_s versus θ_B from equation (6) for fixed $B_z = 15$ mT and varying B_x for two values of λ_{SOC} in the 1/4M phase. Compared with the 1/4M data, we can set a lower bound on SOC of $\lambda_{\text{SOC}} \gtrsim 120$ μeV .

1/2M. In 1/2M, the total magnetic moment includes both valley and spin moments. It is defined as

$$\bar{M} = -\bar{\nabla}_B E_0,$$

where E_0 is the ground-state energy expressed as

$$E_0 = \min \left\{ E(\theta_s, \delta\theta, \delta n) \mid \theta_s \in [0, \pi], \delta\theta \in \left[-\frac{\pi}{2}, \frac{\pi}{2}\right], \delta n \in [-1, 1] \right\}.$$

We expect both $\delta\theta$ and δn to be perturbatively small in $\lambda_{\text{SOC}}/U_{\text{Hu}}$, as indeed confirmed numerically by minimizing the energy E in equation (4). Thus, the energy of 1/2M can be expressed as a function of θ_s as the only variable. We do this by minimizing the expression for E over $\delta\theta$ and δn , and find

$$E_{\text{eff}} \approx \alpha \langle S_z \rangle^2 - \frac{g}{2} \mu_B \bar{B} \cdot \langle \bar{S} \rangle = \alpha \cos^2(\theta_s) - \frac{g}{2} \mu_B B \cos(\theta_s - \theta_B), \quad (7)$$

where

$$\alpha = \left(\frac{\lambda_{\text{SOC}}}{2} \right)^2 \left(\frac{1}{2U_{\text{Hu}}} - \frac{1}{U_{\text{Hu}} + 2\chi_\tau^{-1}} \right) = \frac{\lambda_{\text{SOC}}^2}{8U_{\text{Hu}}} \left(\frac{2\chi_\tau^{-1} - U_{\text{Hu}}}{2\chi_\tau^{-1} + U_{\text{Hu}}} \right) \Big|_{\chi_\tau^{-1} \approx U_{\text{Hu}}} \approx \frac{\lambda_{\text{SOC}}^2}{8U_{\text{Hu}}}, \quad (8)$$

with easy-plane ferromagnet for $\alpha > 0$, and an easy-axis ferromagnet otherwise. Intuitively, the first term of the expression for α comes from the fact that easy-plane ferromagnet gains energy from SOC by canting the spin in each valley in the opposite direction (towards $\langle \tau_z \rangle \cdot \hat{z}$), which comes at the cost of intervalley exchange energy, because the spin moments of the two valleys are not perfectly aligned. The second term is the energy gained by an easy-axis ferromagnet due to SOC. In this case, the system gains energy by generating a finite valley polarization ($\langle \tau_z \rangle \neq 0$). From schF numerical calculations, we derive $\chi_\tau = 15.8$ eV⁻¹. Since $\chi_\tau^{-1} = 63.3$ meV $\gg U_{\text{Hu}}$, the second term is small and, hence, we expect positive α and correspondingly easy-plane spin ferromagnet.

The 1/2M phase (Fig. 4f, solid lines) shows the calculated θ_s versus θ_B by minimizing E_{eff} in equation (7) for various indicated positive and negative values of α for fixed $B_z = 15$ mT and varying B_x . From comparison with the data, we can set an upper bound on $|\alpha| < 0.25$ μeV .

Combining with the derived $\lambda_{\text{SOC}} \gtrsim 120 \mu\text{eV}$ and the numerically attained χ_{T}^{-1} , we can set a lower bound on the interaction energy as

$$U_{\text{Hu}} > 6.5 \text{ meV} \Rightarrow J_{\text{H}} > 3.1 \times 10^{-12} \text{ meV cm}^2,$$

where we used the experimental carrier density, $n = 2.1 \times 10^{12} \text{ cm}^{-2}$. Crucially, this bound is not very sensitive to the numerically extracted value of χ_{T} as long as $\chi_{\text{T}}^{-1} \gg U_{\text{Hu}}$ (equation (8)).

With these parameters, δn is vanishingly small, and hence, the orbital magnetization is negligible. As a result, the magnetization in the 1/2M phase is given by the spin magnetization. Similarly, $\delta\theta$ is very small, and hence, the spin canting is negligible. Note that the attained value of $U_{\text{Hu}} > 6.5 \text{ meV}$ is not much lower than the maximum theoretical value of $U_{\text{Hu}} = V_{q=K}(\epsilon = 1) = 11.2 \text{ meV}$, which is the intervalley Coulomb energy in a vacuum ($\bar{K} = (0, \frac{4\pi}{3})$ is the intervalley wavevector). Note that the dielectric constant at wavevector \bar{K} can be substantially different from the dielectric constant at small wavevectors, which enters the screened Coulomb interaction at the distance between electrons.

In the above discussion, we have assumed momentum-independent Hund's coupling. In the presence of a k -dependent coupling, the anisotropy expression $\alpha \cong \lambda_{\text{SOC}}^2/8U_{\text{Hu}}$ in the limit of $\lambda_{\text{SOC}} \ll U_{\text{Hu}}$ will remain valid, where U_{Hu} should be thought of as momentum-averaged Hund's energy (that is, it remains the average Hund's interaction energy per electron). Our reasoning for the Hund's origin of spin isotropy in 1/2M is as follows: given the fact that the 1/4M phase is fully out-of-plane polarized, we infer that the spin orientation in each valley is dominated by an Ising-like SOC term. In this case, the only way to get an isotropic non-zero spin magnetism in the 1/2M phase is by coupling the spins between the valleys such that they will have a common orientation and the effect of the SOC on each valley will cancel out. The simplest term that has this effect and is allowed by the symmetries of the problem is an intervalley Hund's exchange coupling. We are not aware of any additional symmetry-allowed term that, under reasonable assumptions, can explain the observed spin isotropy in the 1/2M phase.

Experimental determination of isospin tilt angle in 1/2M

The tilt angle of the isospin moment at the M-to-1/2M transition was determined as follows. The magnetic moment distribution $\mathbf{m}(\mathbf{r}) = m(\mathbf{r})\hat{z}$ attained in out-of-plane B_a ($\theta_B = 0$, Extended Data Fig. 7a) is rotated by a trial angle θ_{tr} , $\mathbf{m}(\mathbf{r}) = m(\mathbf{r}) \cos \theta_{\text{tr}}\hat{z} + m(\mathbf{r}) \sin \theta_{\text{tr}}\hat{x}$, and the corresponding $B_z^{\text{tr}}(\mathbf{r}, \theta_{\text{tr}})$ is calculated:

$$B_z^{\text{tr}}(\mathbf{r}, \theta_{\text{tr}}) = \frac{\mu_0}{4\pi} \iint \left[\frac{3\mathbf{m}(\mathbf{r}') \cdot (\mathbf{r} - \mathbf{r}')}{|\mathbf{r} - \mathbf{r}'|^5} (\mathbf{r} - \mathbf{r}') \cdot \hat{z} - \frac{\mathbf{m}(\mathbf{r}') \cdot \hat{z}}{|\mathbf{r} - \mathbf{r}'|^3} \right] dA'.$$

We then calculate the mean squared deviation between the measured $B_z^{\text{ac}}(\mathbf{r})$ in the presence of B_a along a given θ_B (Extended Data Fig. 8b) and the calculated $B_z^{\text{tr}}(\mathbf{r}, \theta_{\text{tr}})$ (Extended Data Fig. 8c), quantified by $\text{Error} = \langle |B_z^{\text{ac}}(\mathbf{r}, \theta_B) - B_z^{\text{tr}}(\mathbf{r}, \theta_{\text{tr}})|^2 \rangle$. We identify the isospin tilt angle θ_s with θ_{tr} that results in minimal error (Extended Data Fig. 8d). The resulting θ_s for various positive and negative θ_B values is presented in Fig. 4f.

In the above procedure, we have made a simplifying assumption that the spin tilt angle θ_s is position independent, whereas disorder and local strain may result in position-dependent magnetic anisotropy. We note that the inversion problem with arbitrary spin orientation has no single-valued mathematical solution, and hence, some constraints must be imposed. We have, therefore, applied the simplest assumption of uniform θ_s that shows a good fit to the experimental data.

To provide an additional assessment of the applicability of this assumption and to test for spatial variations in θ_s , we have repeated the analysis over several narrow strips of the sample (Extended Data Fig. 8e, coloured dashed rectangles). To improve the signal-to-noise ratio, we integrated $B_z^{\text{ac}}(x, y)$ over y within each strip. Extended Data Fig. 8f (red curves) shows the averaged $B_z^{\text{ac}}(x)$ profiles in the three strips attained from Fig. 3g, as compared with the calculated ones shown in

Extended Data Fig. 8e (blue) for the case of $\theta_B = 0$. Extended Data Fig. 8g shows the results of the same procedure for $\theta_B = -45^\circ$. The corresponding error function for the three strips for $\theta_B = -45^\circ$ is shown in Extended Data Fig. 8h. The quality of the fits and the derived uncertainty of the tilt angles θ_s in the three strips is consistent with global values (Extended Data Fig. 8d) within our uncertainty of 5° , suggesting that the variations in the local anisotropy are weak, and the orientation of magnetization can be considered homogeneous.

Our understanding of how strain affects the electronic properties is generally limited, and its impact on magnetic anisotropy is even less understood. In the case of rhombohedral tetralayer graphene, we believe that the strain's effect on local magnetization orientation should be weak. This conclusion is based on our finding that 1/2M is highly isotropic, whereas 1/4M is strongly easy-axis anisotropic. The theoretical curves in Fig. 4f show that substantial variations in α in 1/2M and in λ_{SOC} in 1/4M result in relatively small deviations in the resulting spin orientation θ_s . Therefore, we believe that, in practice, possible strain-induced local variations in the SOC or anisotropy parameter will result in only small local variations in θ_s , unresolvable within our experimental resolution.

Evaluation of isospin texture in the 1/4M phase

Extended Data Fig. 9a shows a schematic of the different components of magnetization vectors at the 1/2M-to-1/4M transition. The measured differential magnetization across the transition, \mathbf{m} (magenta vector), is given by the difference between the magnetization in 1/4M, $\mathcal{M}_{1/4M}$ (blue vector), and 1/2M, $\mathcal{M}_{1/2M}$ (purple): $\mathbf{m} = \mathcal{M}_{1/4M} - \mathcal{M}_{1/2M} = \mathcal{M}_{1/4M}^{\text{O}} + \mathcal{M}_{1/4M}^{\text{S}} - \mathcal{M}_{1/2M}^{\text{S}}$. Here $\mathcal{M}_{1/2M}^{\text{S}}$ is the spin magnetization in 1/2M (purple) oriented along the applied field direction θ_B , and $\mathcal{M}_{1/4M}$ (blue) is given by the sum of the orbital magnetization, $\mathcal{M}_{1/4M}^{\text{O}}$ (brown), oriented along z , and the spin magnetization, $\mathcal{M}_{1/4M}^{\text{S}}$ (green), with a tilt angle θ_s that we aim to determine as follows.

Since the carrier density at the two sides of the 1/2M-to-1/4M transition is the same, the spin magnetization should have the same magnitude ($|\mathcal{M}_{1/2M}^{\text{S}}| = |\mathcal{M}_{1/4M}^{\text{S}}|$; the green and purple vectors are of the same length), and should equal $|\mathcal{M}_{1/2M}^{\text{S}}|$ at the M-to-1/2M transition (Fig. 3j), rescaled by the relative carrier densities at the two transitions and by the partial polarization in the PSP-M region. For out-of-plane B_a ($\theta_B = 0$), $\mathcal{M}_{1/4M}^{\text{S}} = \mathcal{M}_{1/2M}^{\text{S}}$ (the green and purple vectors are parallel), and hence, $\mathbf{m} = \mathcal{M}_{1/4M}^{\text{O}}$. The brown vector is, thus, known and is given by Fig. 4d. We can then evaluate θ_s by comparing the measured $B_z^{\text{ac}}(x, y)$ corresponding to \mathbf{m} (magenta), with $B_z^{\text{ac}}(x, y, \theta_{\text{tr}})$ derived from the summation of the green, brown and purple vectors, $\mathbf{m} = \mathcal{M}_{1/4M}^{\text{O}} + \mathcal{M}_{1/4M}^{\text{S}}(\theta_{\text{tr}}) - \mathcal{M}_{1/2M}^{\text{S}}(\theta_B)$, where θ_{tr} is a trial angle for the spin orientation θ_s in 1/4M (green).

Extended Data Fig. 9b,c shows the measured $B_z^{\text{ac}}(x, y)$ at $\theta_B = 78^\circ$ and the calculated $B_z^{\text{tr}}(x, y, \theta_{\text{tr}})$ using the above procedure, whereas Fig. 4e shows the calculated $B_z^{\text{tr}}(x, y, \theta_{\text{tr}})$ at $\theta_B = 83^\circ$. The corresponding mean square error $\text{Error} = \langle |B_z^{\text{ac}}(x, y) - B_z^{\text{tr}}(x, y, \theta_{\text{tr}})|^2 \rangle$ at $\theta_B = 78^\circ$ is plotted as a function of θ_{tr} (Extended Data Fig. 9d). The minimal error at $\theta_{\text{tr}} = 1.4^\circ$ designates the spin tilt angle ($\theta_{\text{tr}} = \theta_s$) of $\mathcal{M}_{1/4M}^{\text{S}}$ (green vector) and the resulting $B_z^{\text{ac}}(x, y, \theta_{\text{tr}} = \theta_s)$ is shown in Extended Data Fig. 9c. The magenta triangles in Fig. 4f show the average $|\theta_s|$ derived from the above procedure at $\theta_B = \pm 78^\circ$ and $\theta_B = \pm 83^\circ$.

We can attain an additional bound on θ_s in 1/4M as follows. Because the isospin magnetization is isotropic in 1/2M, the spin will be essentially in-plane polarized at large in-plane field B_x . Further increase in B_x will hardly affect the magnetization in 1/2M, but may tilt the spin orientation in 1/4M away from the easy axis. We first apply a small $B_z = 15 \text{ mT}$ and a large $B_x = 70 \text{ mT}$ ($\theta_B = 78^\circ$) and acquire the corresponding $B_z^{\text{ac}}(x, y)$ across the 1/2M-to-1/4M transition. The in-plane field is then set to $B_x = -70 \text{ mT}$ and the resulting $B_z^{\text{ac}}(x, y)$ is measured. The two sets of data are subtracted, with the difference, $B_z^{\text{ac}\pm}(x, y) = B_z^{\text{ac}+}(x, y) - B_z^{\text{ac}-}(x, y)$, presented in Extended Data Fig. 9e. This procedure eliminates the out-of-plane component of the differential magnetization, which is independent of the B_x direction,

with $B_z^{ac\pm}(x, y)$ reflecting only the stray field due to the in-plane component of differential magnetization across the transition. The same procedure is repeated with substantially larger $B_x = \pm 120$ mT ($\theta_B = 83^\circ$), with the resulting $B_z^{ac\pm}(x, y)$ presented in Extended Data Fig. 9f. Extended Data Fig. 9g presents the difference $\Delta B_z^{ac}(x, y) = B_z^{ac\pm}(x, y)_{120\text{ mT}} - B_z^{ac\pm}(x, y)_{70\text{ mT}}$, which shows that the change in differential in-plane magnetization across the transition, and hence the possible change in the isospin orientation in the 1/4M, are unresolvable between the two B_x values within our resolution. By averaging over the y axis for improved signal-to-noise ratio of the $B_z^{ac\pm}(x, y)_{120\text{ mT}}$ data (red) and the $\Delta B_z^{ac}(x, y)$ data (black) in Extended Data Fig. 9h, we can estimate that the change in in-plane magnetization is less than 9%, placing an upper bound on possible spin tilt angle change in 1/4M between $B_x = 70$ mT and $B_x = 120$ mT of about 5° , which we use as the error bar for θ_s in the 1/4M phase (Fig. 4f).

Reconstruction of 2D isospin magnetization

To reconstruct the out-of-plane magnetization, instead of the Tikhonov-regularized Fourier-transform-based approach⁵⁸, we use a numerical method based on a deep neural network, similar to that in ref. 59. In this method, we consider a three-layer network architecture, consisting of the input layer, deep layer and recovered image layer. Both deep layer and recovered image layer utilize the rectified linear unit activation function. The recovered image layer represents the magnetization m . The convolution of the recovered image layer with the Biot–Savart kernel yields $B_{z,\text{sim}}^{ac}$, the magnetic field predicted by the network. To achieve faster convergence, the input layer is initialized with the measured values of $B_z^{ac}(x, y)$. The network's weights are optimized by minimizing the merit function as

$$f_M = \|B_{z,\text{sim}}^{ac} - B_z^{ac}\|^2 + \lambda_\alpha \|\nabla^2 m\|^2,$$

which ensures that the theoretical magnetic field closely matches the measured field and maintains smoothness in magnetization. Here λ_α is the Tikhonov regularization parameter.

Data availability

The experimental data used in this work are available at <https://doi.org/10.34933/758cd790-2d69-4b2b-952b-96305adbe9e2>.

Code availability

The sCHF, anisotropy and magnetic inversion calculations used in this study are available from the corresponding author on reasonable request.

References

- Yang, Y. et al. Stacking order in graphite films controlled by van der Waals technology. *Nano Lett.* **19**, 8526–8532 (2019).
- Li, Y. et al. Probing symmetry properties of few-layer MoS₂ and h-BN by optical second-harmonic generation. *Nano Lett.* **13**, 3329–3333 (2013).
- Shan, Y. et al. Stacking symmetry governed second harmonic generation in graphene trilayers. *Sci. Adv.* **4**, eaat0074 (2018).
- Anahory, Y. et al. SQUID-on-tip with single-electron spin sensitivity for high-field and ultra-low temperature nanomagnetic imaging. *Nanoscale* **12**, 3174–3182 (2020).
- Finkler, A. et al. Scanning superconducting quantum interference device on a tip for magnetic imaging of nanoscale phenomena. *Rev. Sci. Instrum.* **83**, 073702 (2012).
- Huber, M. E. et al. d.c. SQUID series array amplifiers with 120 MHz bandwidth. *IEEE Trans. Appl. Supercond.* **11**, 1251–1256 (2001).
- Meltzer, A. Y., Levin, E. & Zeldov, E. Direct reconstruction of two-dimensional currents in thin films from magnetic-field measurements. *Phys. Rev. Appl.* **8**, 064030 (2017).

- Dubois, A. E. E. et al. Untrained physically informed neural network for image reconstruction of magnetic field sources. *Phys. Rev. Appl.* **18**, 064076 (2022).

Acknowledgements

We thank A. F. Young for fruitful discussions. This work was co-funded by the Minerva Foundation grant number 140687, by the United States–Israel Binational Science Foundation (BSF) grant number 2022013, by the Institute for Artificial Intelligence, and by the European Union (ERC, MoireMultiProbe 101089714). Views and opinions expressed are, however, those of the author(s) only and do not necessarily reflect those of the European Union or the European Research Council. Neither the European Union nor the granting authority can be held responsible for them. E.Z. acknowledges support from the Andre Deloro Prize for Scientific Research, Goldfield Family Charitable Trust, and Leona M. and Harry B. Helmsley Charitable Trust grant number 2112-04911. Y.O. acknowledges support from the European Union's Horizon 2020 research and innovation programme (grant agreement LEGOTOP number 788715), the DFG (CRC/Transregio 183, EI 519/7-1) and the Israel Science Foundation ISF (grant number 1914/24). E.B. acknowledges support from the ERC under grant HQMAT (grant agreement number 817799), and from an NSF-BSF award number DMR-2000987. T.H. acknowledges financial support from the ERC under grant QuantumCUSP (grant agreement number 101077020). K.W. and T.T. acknowledge support from the JSPS KAKENHI (grant numbers 21H05233 and 23H02052), the CREST (JPMJCR24A5), JST and World Premier International Research Center Initiative (WPI), MEXT, Japan.

Author contributions

N.A. designed and built the SOT microscope and S.G. advanced the software. S.D. and N.A. performed the local magnetization studies. M.U. fabricated and characterized the samples. M.U., N.A. and S.D. performed the transport measurements and data analysis. S.D., N.A., M.U. and E.Z. designed the experiment. S.D. and Y.M. fabricated the SOT and tuning fork, and M.E.H. developed the SOT read-out. Y.V., T.H., P.E., Y.O. and E.B. performed the theoretical modelling. Y.V., S.D., Y.Z. and N.A. performed the sCHF, Stoner and phase diagram calculations. Y.V. and S.D. performed the Hund's and SOC modelling and calculations. S.D., Y.Z. and P.E. performed the LL calculations. A.Y.M. developed the magnetization reconstruction algorithm. S.D., Y.Z. and A.Y.M. carried out the anisotropy analysis. K.W. and T.T. provided the hBN crystals. S.D., N.A., M.U., Y.V., T.H. and E.Z. wrote the original paper. All authors participated in discussions and revisions of the paper.

Competing interests

The authors declare no competing interests.

Additional information

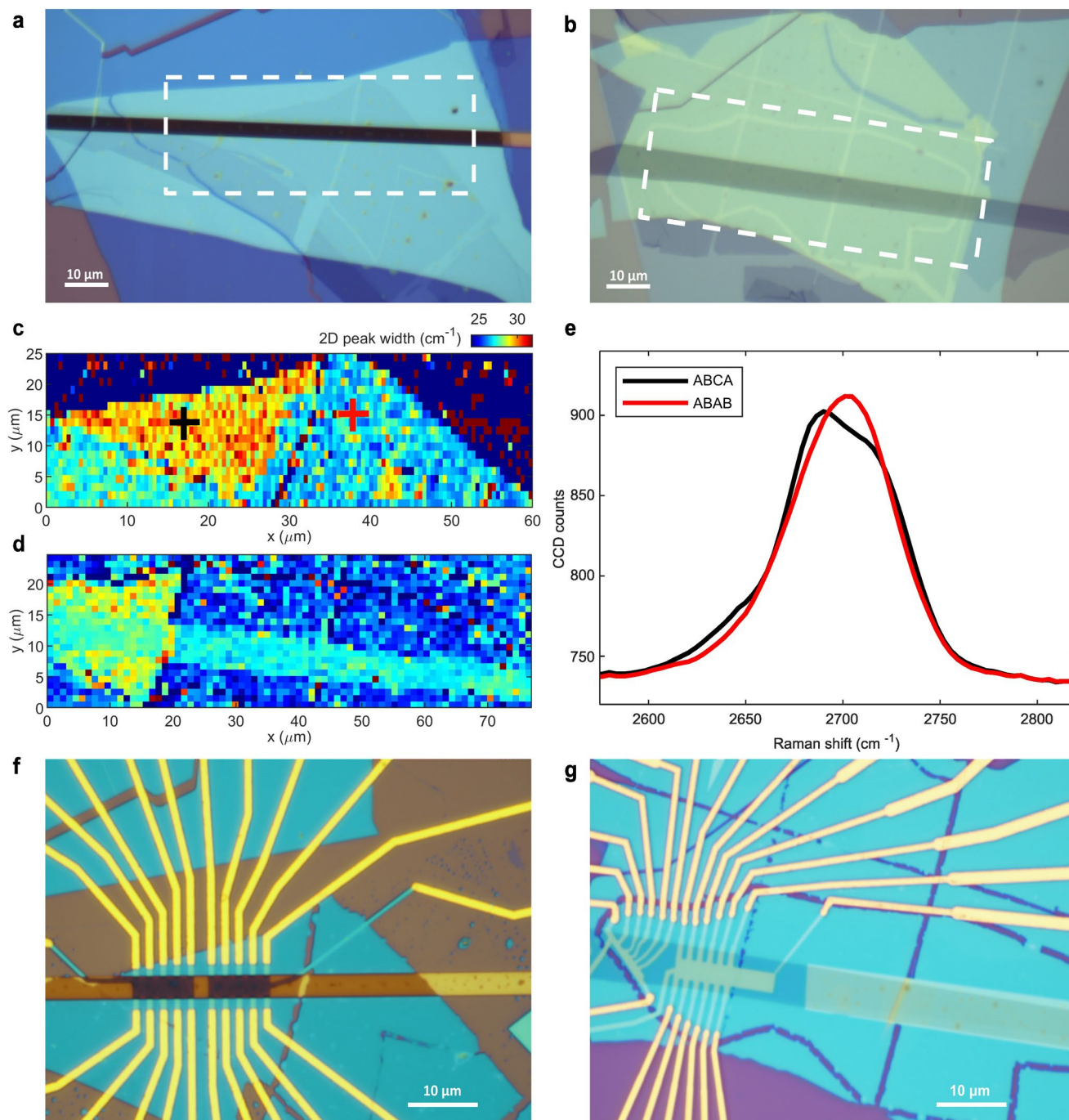
Extended data is available for this paper at <https://doi.org/10.1038/s41567-025-03035-z>.

Supplementary information The online version contains supplementary material available at <https://doi.org/10.1038/s41567-025-03035-z>.

Correspondence and requests for materials should be addressed to Eli Zeldov.

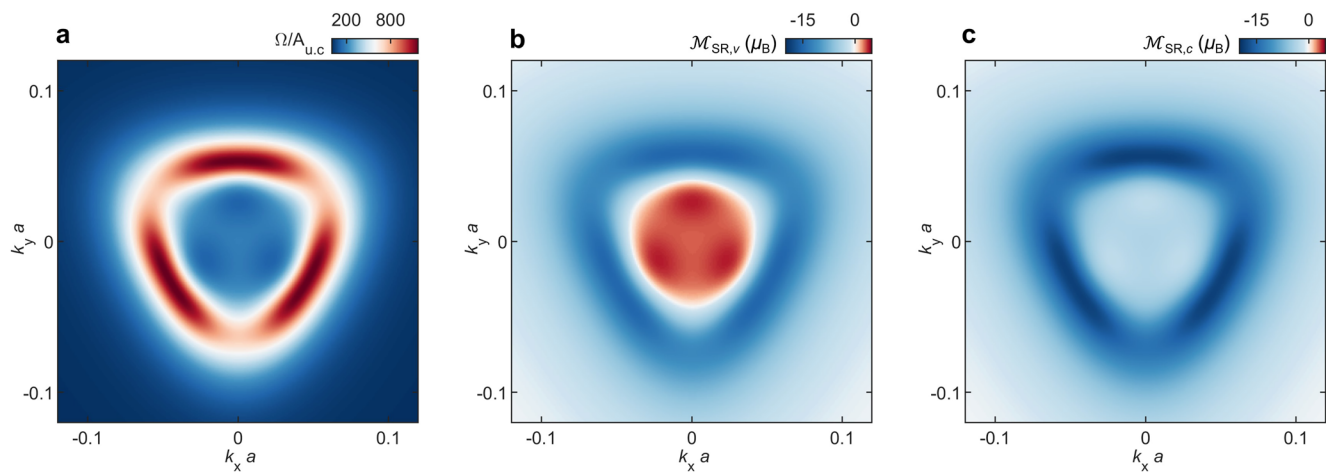
Peer review information *Nature Physics* thanks Martino Poggio and the other, anonymous, reviewer(s) for their contribution to the peer review of this work.

Reprints and permissions information is available at www.nature.com/reprints.

**Extended Data Fig. 1 | Device fabrication of rhombohedral graphene.**

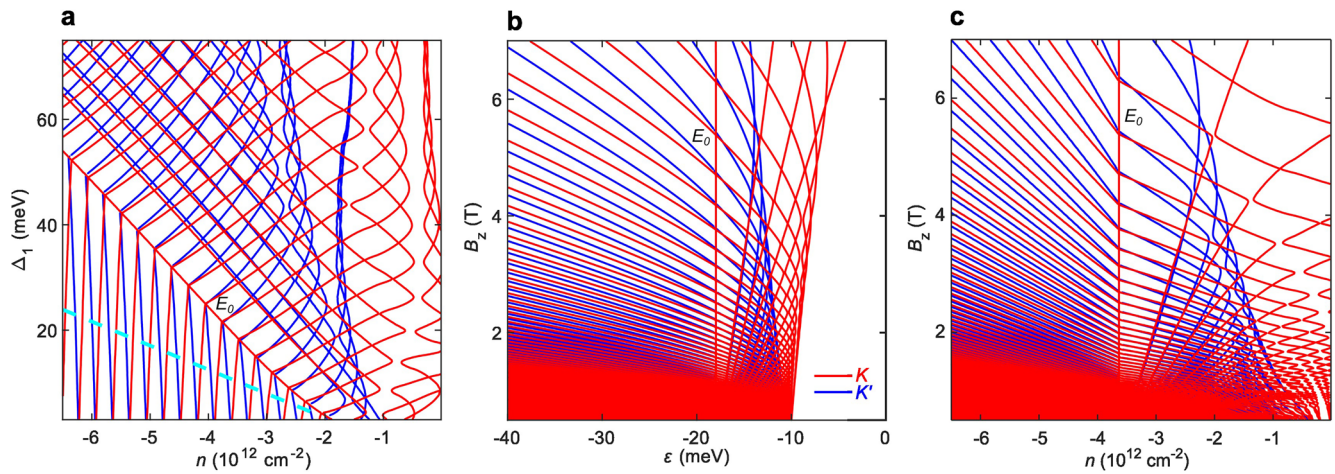
a, Optical image of the hBN/ABCA Graphene/hBN stack (blue) on Si/SiO₂ substrate (gray-brown) with Ti/Pt bottom gate (dark brown) for device B. **b**, Same as (a) for devices A and C. **c**, Raman map of the Gaussian-fitted width of the 2D peak in the dashed rectangle in (a). The yellow-red triangular region corresponds to ABCA graphene stacking, and the blue-green regions correspond to ABAB

stacking, separated by sharp domain walls. **d**, Same as (c) for the region marked by the dashed rectangle in (b). **e**, Typical 2D peaks of the Raman spectrum for the two stacking configurations measured at the points marked by black and red crosses in (c). The ABAB 2D peak is narrower and more symmetric than the ABCA 2D peak. **f**, Optical image of the final device B (right Hall bar). **g**, Final devices A (left) and C (right).



Extended Data Fig. 2 | Berry curvature and orbital magnetism in rhombohedral ABCA graphene. **a**, Momentum dependent Berry curvature $\Omega(k)$ in valley K in the valence band for $\Delta_1 = 10$ meV. **b**, Self-rotation component of the orbital magnetization in K valence band, $\mathcal{M}_{SR,v}(k)$, with positive values

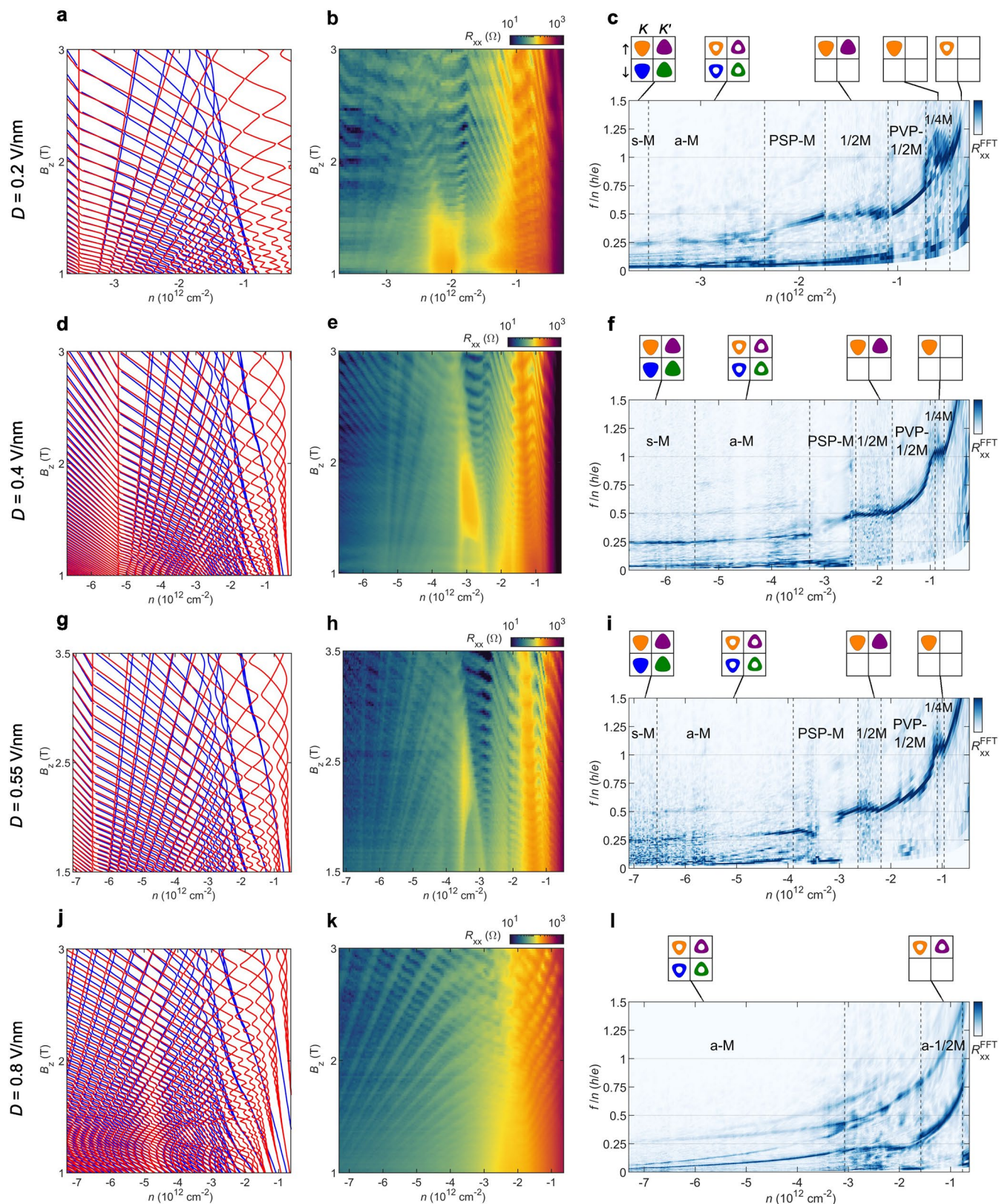
near zero k and negative values at larger momenta. **c**, Same as **(b)** in the conduction band, $\mathcal{M}_{SR,c}(k)$, with negative values for all k . In K' valley the $\Omega(k)$ and $\mathcal{M}_{SR,n}(k)$ are rotated by 180° and have an opposite sign.



Extended Data Fig. 3 | Calculated Landau levels in the valence band.

a, Evolution of the LLs with n and Δ_1 in valleys K (red) and K' (blue) at $B_z = 3$ T, attained within single particle band structure calculations. The TMBR gives rise to valley polarization and corresponding degeneracy lifting of the LLs. At low carrier densities a full polarization occurs with only K LLs present (red). The red line labeled E_0 is the 0th K LL that resides at $k = 0$ and coincides with the annulus

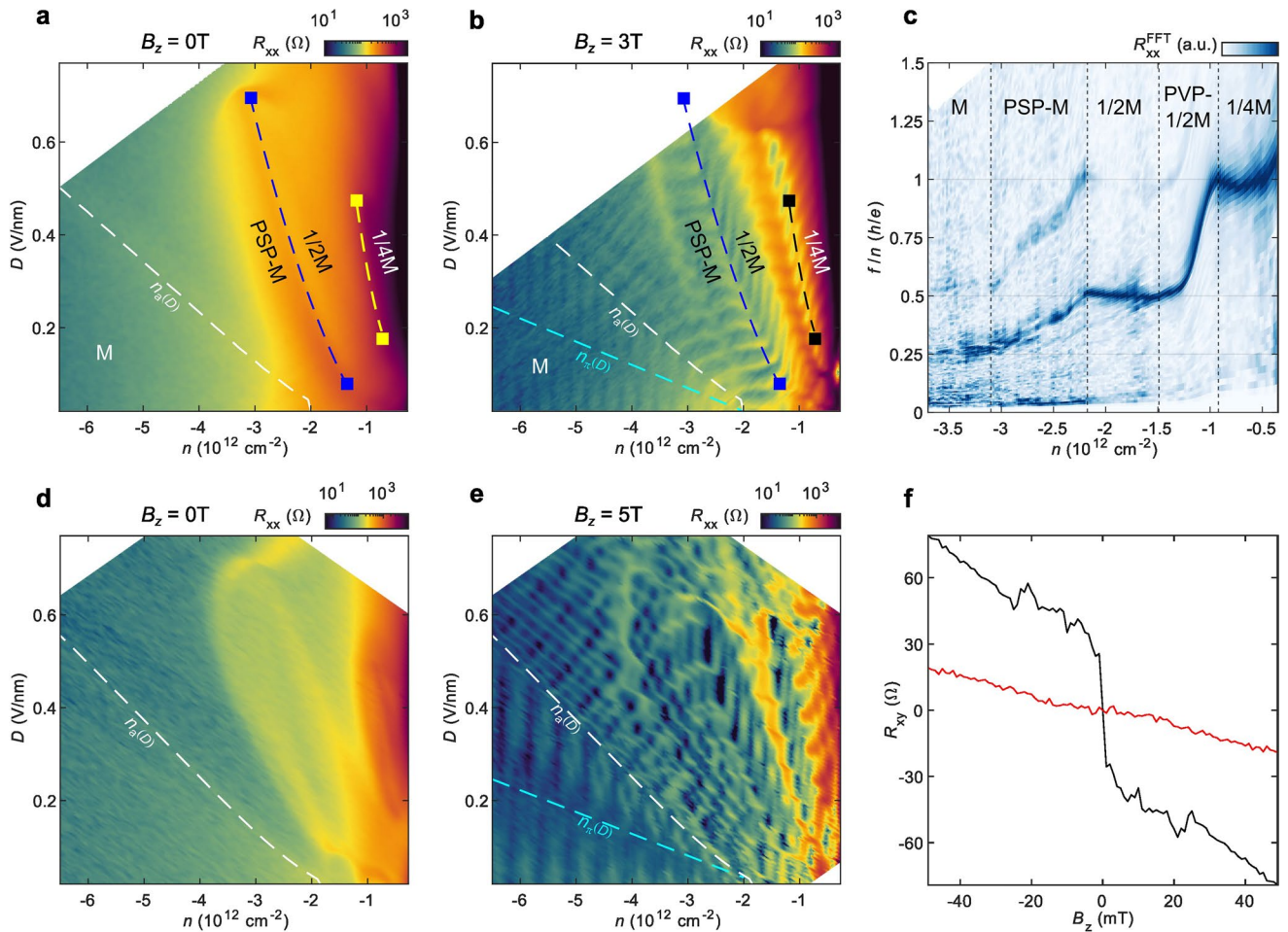
opening line $n_a(D)$. The cyan dashed line is the $n_n(D)$ line, which traces the positions where the K and K' LLs acquire a relative shift of half a period. These calculated $n_a(D)$ and $n_n(D)$ lines are plotted in Fig. 1d–f. **b**, Evolution of the LLs with ϵ and B_z for $\Delta_1 = 20$ meV. **c**, Evolution of the LLs with n and B_z for $\Delta_1 = 20$ meV.



Extended Data Fig. 4 | Analysis of quantum oscillations in R_{xx} in device A.

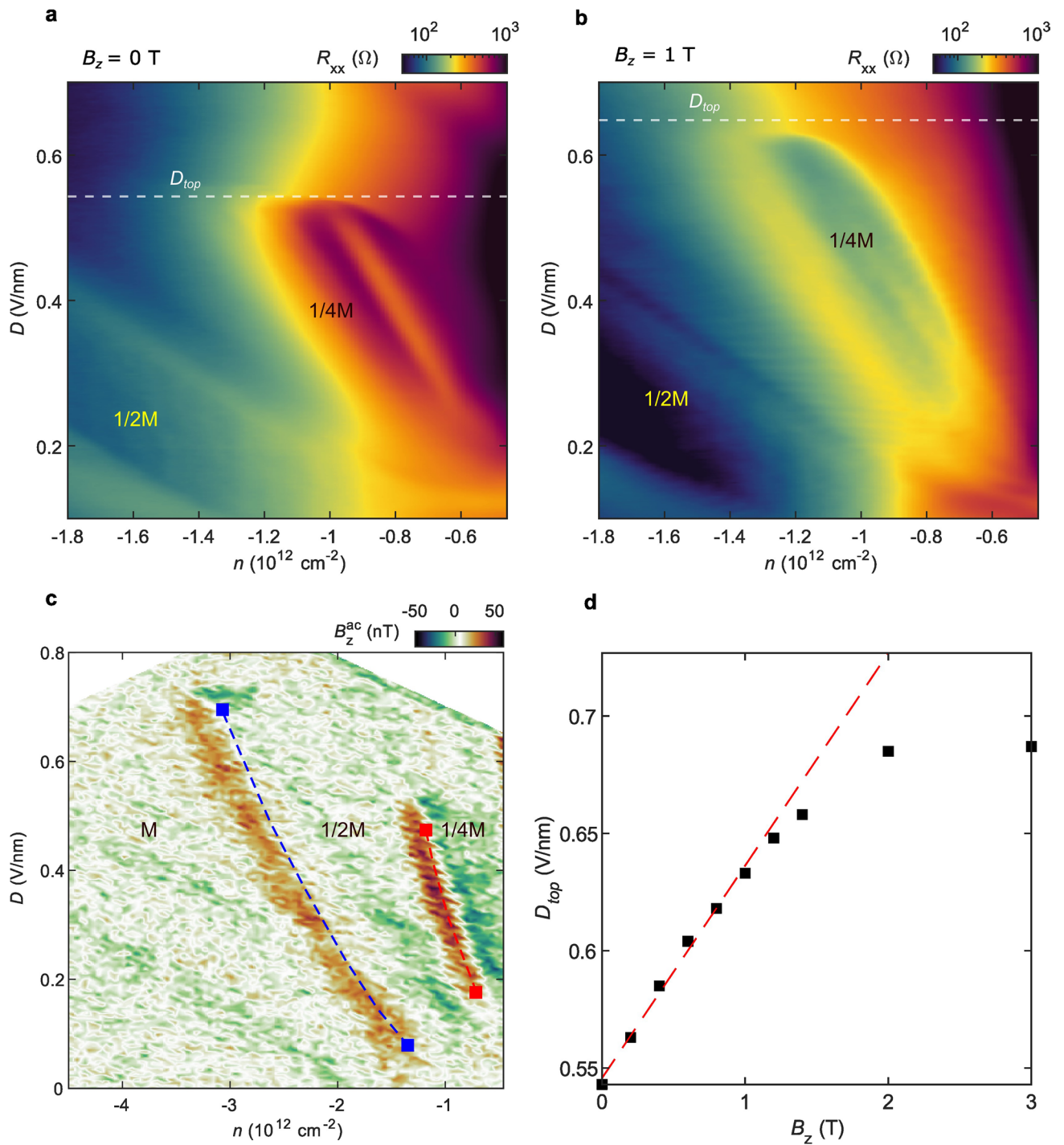
a, Calculated LLs in K (red) and K' (blue) valleys vs. n and B_z at $D = 0.2$ V/nm within single particle band structure. **b**, Measured $R_{xx}(n, B_z)$ at $D = 0.2$ V/nm. At $|n| \gtrsim 2.4 \times 10^{12} \text{ cm}^{-2}$ the QOs are well described by single particle calculations in (a), whereas at lower densities a sequence of interaction-driven symmetry breaking transitions occurs. **c**, Fast Fourier transform (FFT) spectrum

of $R_{xx}(l/B_z)$ vs. n with the normalized frequency f/n presented in units of h/e . The schematics at the top show the occupied hole states in the four flavors. **d-f**, Same as (a-c) at $D = 0.4$ V/nm. **g-i**, Same as (a-c) at $D = 0.55$ V/nm. **j-l**, Same as (a-c) at $D = 0.8$ V/nm. At high displacement field all the accessible range of carrier densities is described by annular Fermi surfaces.



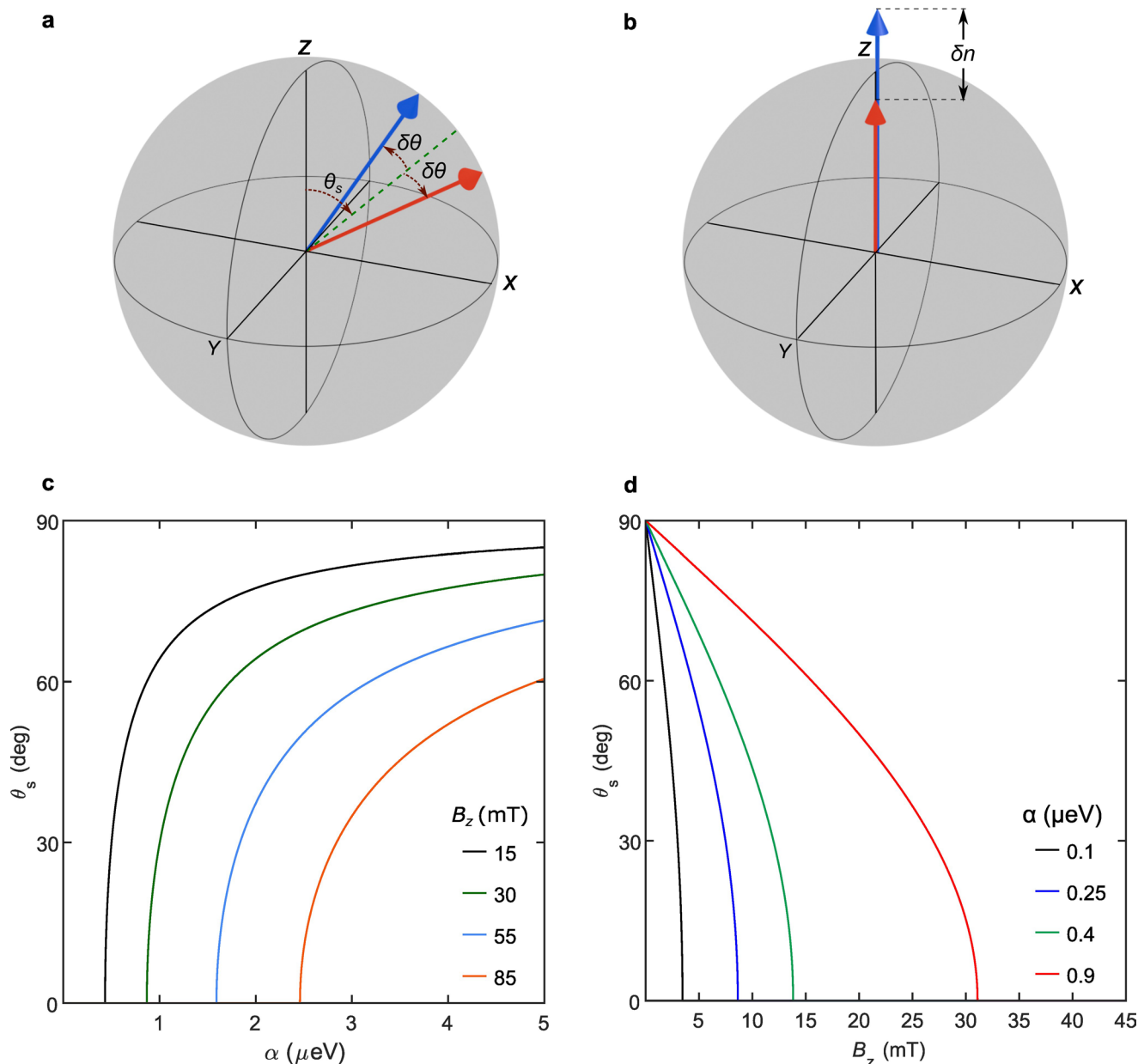
Extended Data Fig. 5 | Transport properties of devices B and C. **a**, $R_{xx}(n, D)$ of device B measured at $B_z = 0 \text{ T}$. The white dashed curve is the $n_a(D)$ line derived from single particle calculations. Blue and yellow lines are M-to-1/2M and 1/2M-to-1/4M transition lines obtained from local magnetization measurements at low field in Fig. 2a. **b**, Same as (a) at $B_z = 3 \text{ T}$. The cyan dashed curve is $n_\pi(D)$ line derived from single particle calculations. The blue local magnetization transition line closely follows the PSP-M-to-1/2M transition observed in transport. The 1/4M

phase at 3 T is seen to expand to slightly higher $|n|$ and considerably larger D as compared to the low-field 1/2M-to-1/4M transition line (black dashed curve). **c**, FFT of the QOs of $R_{xx}(1/B_z)$ vs. n measured at $D = 0.33 \text{ V/nm}$. The FFT frequency is normalized with respect to Hall carrier density n_{Hall} . **d, e**, $R_{xx}(n, D)$ of device C measured at $B_z = 0 \text{ T}$ (d) and 5 T (e). **f**, Low-field Hall resistance R_{xy} vs. B_z in device B measured in the 1/2M phase (red line) and in the 1/4M (black line) showing AHE.



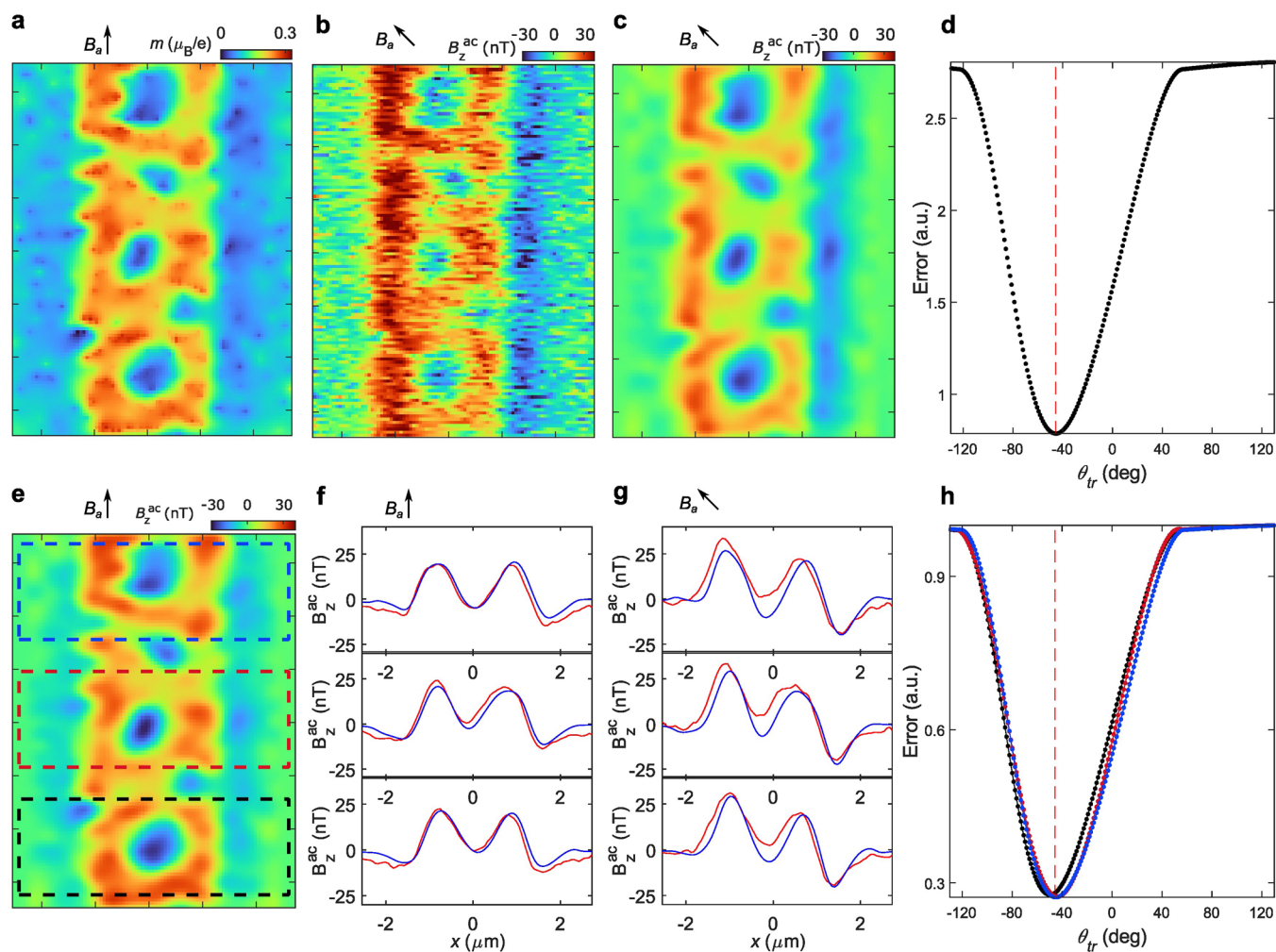
Extended Data Fig. 6 | Expansion of the 1/4M phase with magnetic field.
a, Measured $R_{xx}(n, D)$ in device A at $B_z = 0$ T. The dashed line marks the top endpoint D_{top} of the 1/4M phase. **b**, Same as (a) at $B_z = 1$ T. **c**, $B_z^{ac}(n, D)$ measured in device B at $B_z = 356$ mT. The blue and red curves show the locations of the

M-to-1/2M and 1/2M-to-1/4M transition lines at $B_z = 10$ mT derived from Fig. 2b. **d**, Dependence of D_{top} on B_z , showing the upward expansion of the 1/4M phase on expense of 1/2M.



Extended Data Fig. 7 | Spin orientation in 1/2M. a, b, Schematics of valley-spin polarization vectors (\bar{S}_+) (blue) and (\bar{S}_-) (red) for the easy-plane (**a**) and easy-axis (**b**) ferromagnets in the presence of small SOC and finite B_z . **c**, Spin orientation θ_s vs. anisotropy parameter $\alpha \geq 0$ (easy-plane) calculated from equation 7 in 1/2M for $B_x = 0$ and various indicated values of B_z . The black line shows that for the experimentally used $B_z = 15$ mT the spin remains along \hat{z} for anisotropy α below a critical $\alpha_c = 0.43$ μeV , above which the spin unlocks abruptly from \hat{z} orientation and rapidly rotates towards \hat{x} axis ($\theta_s = 90^\circ$). The data in Fig. 4f show that for

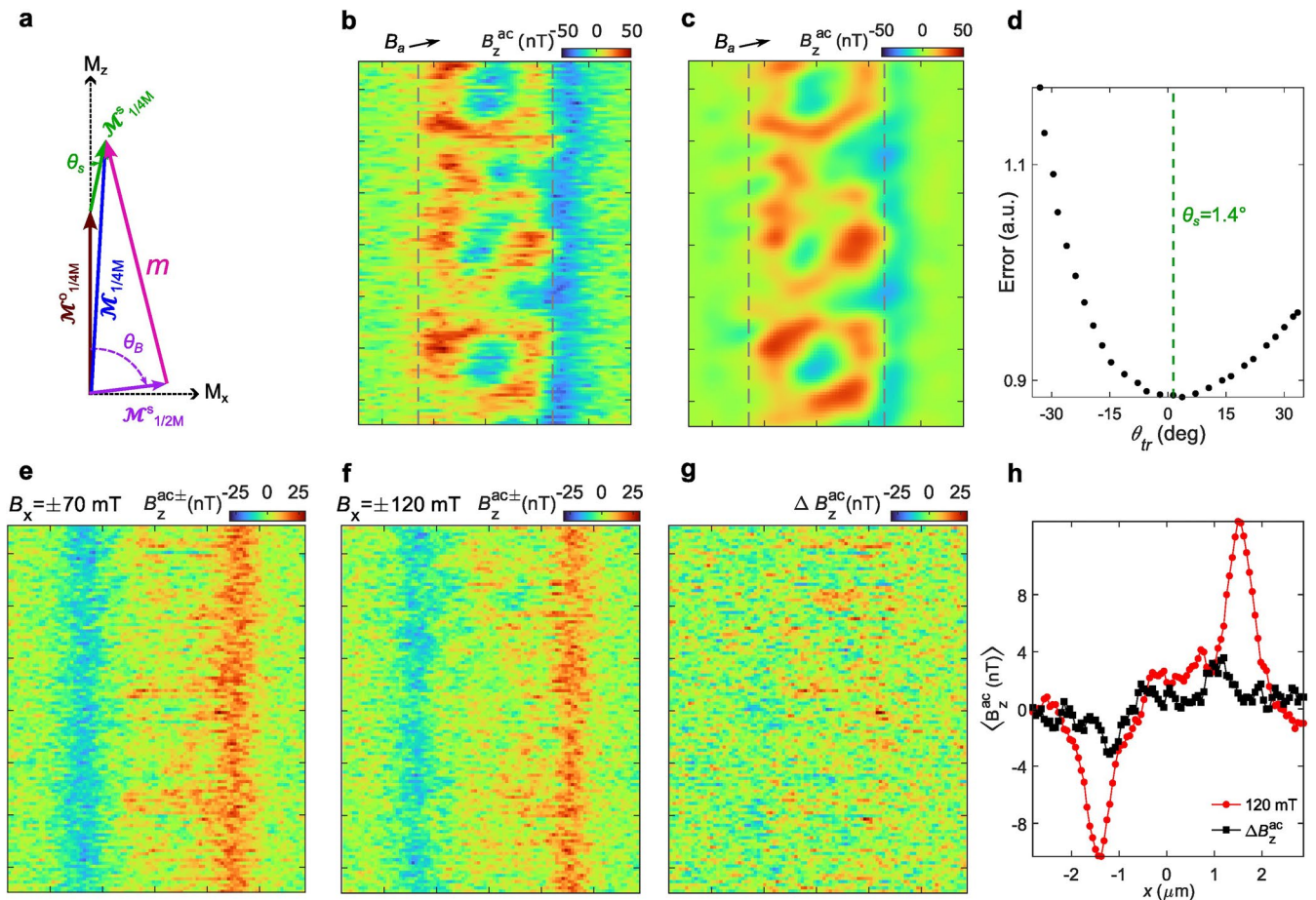
$\theta_B = 0^\circ$ with $B_z = 15$ mT and $B_x = 0$, the measured magnetization is along \hat{z} , which means that $\alpha \leq \alpha_c$. For larger B_z (green, blue, and red curves) the spin remains locked to \hat{z} up to higher values of α_c . **d**, Spin orientation θ_s vs. B_z for $B_x = 0$ and various anisotropy values α . For small α , the B_z rapidly rotates the spin from the easy plane orientation ($\theta_s = 90^\circ$) towards the \hat{z} axis ($\theta_s = 0^\circ$). With increasing anisotropy, the in-plane magnetization survives up to higher B_z (colored lines).



Extended Data Fig. 8 | Determining isospin tilt angle at M-to-1/2M transition.

a, Reconstructed differential magnetization $m(x, y)$ in presence of $B_a = B_z$ ($\theta_B = 0$) reproduced from Fig. 3j. **b**, $B_z^{ac}(x, y)$ measured at M-to-1/2M transition (black star in Fig. 2a) at $\theta_B = -45^\circ$ (Fig. 3i). **c**, Calculated $B_z^{ac}(x, y, \theta_{tr})$ for $\theta_{tr} = -45.6^\circ$, at which the mean squared deviation between (b) and (c) is minimal. **d**, Plot of the mean squared error vs. the trial angle θ_{tr} . The dashed line marks $\theta_{tr} = -45.6^\circ$ with the minimal error, which defines the spin tilt angle θ_s .

e, Calculated $B_z^{ac}(x, y)$ from $m(x, y)$ in (a) for $\theta_B = 0^\circ$. **f**, Comparison between the measured $B_z^{ac}(x)$ profiles in Fig. 3g (red) and the computed ones in (e) (blue), averaged along y in the three dashed-border rectangular strips marked in (e). **g**, Same as (f) comparing the averaged measured $B_z^{ac}(x)$ from (b) (red) with the calculated one from (c) (blue). **h**, The mean squared error as in (d) computed for the three strips marked in (e). Red dashed line marks $\theta_{tr} = \theta_s = -45.6^\circ$.



Extended Data Fig. 9 | Analysis of isospin orientation at the 1/2M-to-1/4M transition. **a**, Schematic vector representation of isospin moments at 1/2M-1/4M transition in a tilted magnetic field with angle θ_B . **b**, Measured $B_z^{ac}(x, y)$ at 1/2M-1/4M transition for B_a along $\theta_B = 78^\circ$. **c**, Trial $B_z^{ac}(x, y, \theta_{tr})$ calculated from the vector analysis in **(a)** for $\theta_{tr} = 1.4^\circ$. **d**, Plot of the mean square error vs. the trial angle θ_{tr} . The green dashed line marks $\theta_{tr} = 1.4^\circ$ with the minimal error, which defines the tilt angle θ_s of $M_{1/4M}^s$ (green vector in **(a)**). **e**, $B_z^{ac\pm}(x, y)$ in presence of

a small $B_z = 15$ mT, obtained by subtracting $B_z^{ac-}(x, y)$ measured in presence of in-plane magnetic field $B_x = -70$ mT from $B_z^{ac+}(x, y)$ acquired at $B_x = 70$ mT. **f**, Same as **(a)** at $B_x = 120$ mT. **g**, The difference $\Delta B_z^{ac}(x, y)$ between **(a)** and **(b)**. **h**, $B_z^{ac\pm}(x)$ from **(b)** averaged over y axis (red), and $\Delta B_z^{ac}(x)$ from **(c)** averaged over y (black), allowing estimation of the upper bound of the isospin tilt angle in the 1/4M phase of about 5° .